

1 **Revision 2**

2 **Apatite as an archive of pegmatite-forming processes: an example** 3 **from the Berry-Havey pegmatite (Maine, USA)**

4

5 Word count: 9221 (without references)

6

7 Encarnación Roda-Robles¹, Alfonso Pesquera¹, Pedro Pablo Gil-Crespo¹, William

8 Simmons², Karen Webber², Alexander Falster², Jon Errandonea-Martin¹, Idoia Garate-Olave¹

9

10 ¹*Department of Geology, University of the Basque Country (UPV/EHU), Barrio Sarriena*
11 *s/n, 48940-Leioa, Bizkaia, Spain*

12 ²*Maine Mineral and Gem Museum, PO Box 500, 99 Main Street, Bethel, Maine 04217*

13

14

ABSTRACT

15 Apatite is an accessory phase in all the units of the internally zoned Berry-Havey
16 complex pegmatite. This body presents a highly fractionated core zone, enriched in Li, F, B,
17 Be and P, which hosts three different types of pockets, some of them often containing tens to
18 hundreds of gemmy euhedral Li-rich tourmaline crystals, together with other mineral phases
19 such as lepidolite. Processes involved in the complex internal evolution of pegmatitic melts
20 that give rise to zoned bodies containing pockets are not completely understood. In order to
21 shed light on these processes, apatite from all the different units of the Berry-Havey
22 pegmatite (wall zone, intermediate zone, core margin and core zone pods) and from the
23 three pocket types (Li-poor, Li-rich and apatite seams) has been characterized
24 petrographically and later analyzed for major (electronic microprobe) and trace elements (LA-
25 ICP-MS). Results indicate that apatite chemistry changed significantly during the
26 crystallization of the Berry-Havey pegmatite, reflecting the conditions at each stage and
27 mainly depending on the fractionation degree, fO_2 , and paragenetic association.

28 Fluorapatite is found in all the units except the core margin, the Li-poor pockets and the
29 seams, where Mn-bearing fluorapatite is present. A gradual increase of the Mn content in
30 apatite from the pegmatite border (wall zone) inwards, up to the formation of subrounded
31 masses of Mn-Fe phosphate in the core zone pods, parallels the increasing fractionation of
32 the melt. Phosphate crystallization would deplete the residual melt in Mn, probably causing
33 the significant Mn-decrease observed in apatite from the core zone pods and Li-rich pockets.
34 The late depletion of Mn could also be related to an increase of fO_2 in the melt during the
35 later stages of its evolution.

36 Main trace element variations in apatite at both, pegmatite and crystal scales,
37 correspond to REE, Y and Sr. Yttrium and REE behave in a very similar way, decreasing
38 inwards, i.e. with fractionation of the pegmatitic melt (Σ REE from 1796 ppm in the apatite
39 from the wall zone to 0 ppm in the core zone; and Y from 1503 ppm in the apatite from the
40 wall zone to 0 ppm in the core zone); which could be due to early crystallization of REE-
41 bearing phosphates such as monazite and xenotime. Strontium shows a more complex
42 trend, with an initial depletion in apatite from the wall zone (52 ppm) to the intermediate zone
43 (3 ppm) and a pronounced increase from the core margin (23-87 ppm) up to the core zone
44 and pockets (up to 2.87 wt%). This increase of Sr at the latest fractionation stages of the
45 pegmatite is interpreted to be associated with a late incompatible character of this element in
46 highly fractionated melts, related to the composition of feldspars from the core margin
47 (mainly pure albite). The lack of Ca in feldspars would decrease affinity for Sr incorporation
48 into their structure and, consequently, Sr would go preferentially to apatite in the core zone
49 pods and, more markedly, in the pockets.

50 Apatite also records changes in the redox conditions during crystallization, with the
51 highest fO_2 at the end of the crystallization, mainly reflected in the Eu and Ce anomalies. The
52 chemistry of apatite also reflects the evolution of the pegmatitic melt during crystallization
53 regarding the fluids saturation and pockets generation. Accordingly, at least two exsolution
54 events took place during the Berry-Havey crystallization history: (i) at the beginning of the
55 core zone crystallization, giving rise to the Li-poor pockets; and (ii) after the crystallization of
56 the Li-rich pods of the core zone, resulting in the Li-rich pockets. The apatite-rich seams may

57 have crystallized between these two exsolution events, or later, at a subsolidus stage, after a
58 Na-autometasomatism episode.

59 This study shows how a detailed petrographic and chemical characterization of apatite
60 associated with different units of a highly fractionated, internally zoned pegmatite may help
61 understand the crystallization history of pegmatitic melts. It is also evidenced that during the
62 internal evolution of pegmatites, apatite chemistry records variations in the fO_2 , elemental
63 fractionation, interaction with competing mineral phases, fluids activity and exsolution events.
64 In addition, it is shown how apatite chemistry may be useful as an exploration tool for
65 pegmatites.

66

67 *Keywords: Berry-Havey pegmatite, Maine, apatite, internal fractionation, pockets*
68 *formation*

69

70

INTRODUCTION

71 The Oxford pegmatite field is characterized by the occurrence of some complexly zoned,
72 highly evolved granitic pegmatites. The Berry-Havey is one of the best examples of these
73 bodies that are enriched in incompatible elements (namely Li, F, B, Be and P) in their most
74 fractionated units. This pegmatite presents a well-developed internal zoning, with textural
75 and chemical changes from the contact with the country rocks inward. In addition, numerous
76 miarolitic cavities (pockets) that contain abundant euhedral crystals of gemmy tourmaline,
77 among other phases, are common in the inner zones of this pegmatite. The crystallization
78 history of the Berry-Havey is, therefore, presumed to be complex. Actually, the internal
79 evolution of pegmatitic melts mainly in heterogeneous zoned bodies is not completely
80 understood. Numerous studies on pegmatite fields have been carried out worldwide, as well
81 as experimental work (e.g. Jahns and Burnham, 1969; Veksler et al. 2002; London, 2005), to
82 understand and decipher the characteristics and formation mechanisms of complex
83 pegmatites. In this regard, micas, feldspars, tourmaline and, to a lesser extent, garnet, Fe-
84 Mn-phosphates, Nb-Ta oxides and quartz have been used as petrogenetic indicators to
85 unravel the internal evolution of pegmatitic bodies (e.g., Černý, 1982; London, 2008; Roda-

86 Robles et al. 2012, 2015a, b; Hernández-Filiberto et al. 2021; Müller et al. 2021). In the
87 Berry-Havey pegmatite, textural and chemical variations observed in tourmaline and mica
88 occurring in all the zones of the body are indicative of the crystallization of a strongly
89 fractionated melt from the borders inward (Roda-Robles et al. 2015a, b). Chemical data from
90 apatite presented in this study are consistent with this model. However, chemical variations
91 in this phosphate are more complex and difficult to interpret in comparison to those of
92 tourmaline and mica, probably due to the stronger influence of parameters such as fO_2 or
93 melt polymerization on apatite composition. Thus, a detailed study of the apatite chemistry
94 may be key to understanding the complex crystallization history of this pegmatite. In this
95 paper we present the results of the petrographic and chemical study of apatite associated
96 with the different zones of the Berry-Havey pegmatite and discuss their implications for its
97 petrogenesis. Likewise, the usefulness of apatite as an archive of pegmatite-forming
98 processes and as an exploration tool for fractionated pegmatites is highlighted.

99

100

GEOLOGICAL SETTING

101 The Berry-Havey pegmatite belongs to the Oxford pegmatite field, which is located SW
102 of the state of Maine (USA). This field outcrops in the middle-south area of the “Central
103 Maine Belt” (CMB), a large NE–SW trending synclinorium (Reusch and Staal, 2011) that
104 constitutes the main tectonostratigraphic unit of the northern Appalachians. The CMB is
105 bordered by the Norumbega Shear Zone System to the SE, which puts the CMB in contact
106 with the Neoproterozoic to Silurian rocks of the Avalon Composite Terrain; whereas to the
107 NW this belt is bordered by the Ordovician rocks of the Bronson Hill Belt (Guidotti, 1989;
108 Solar and Tomascak, 2001) (Fig. 1). The CMB is composed of a Lower Paleozoic
109 sedimentary succession together with igneous rocks (e. g. Osberg 1978; Solar and Brown
110 2001). During the Acadian orogeny the CMB was deformed and metamorphosed
111 (greenschist in the NE to upper amphibolite facies and migmatite to the SW, Guidotti, 1989;
112 1993) (Fig. 1), and also intruded by Devonian to Permian plutons (e.g. Moench et al. 1995;
113 Bradley et al. 1998; Solar and Brown, 2001, Solar and Tomascak, 2016).

114 Most pegmatites from the Oxford field concentrate on the northern and eastern margins
115 of the so-called “Migmatite-Granite complex” (MGC) (previously known as Sebago Migmatite
116 Domain (Solar and Tomascak, 2016)). The MGC, located in the core of the CMB, presents a
117 high metamorphic set of facies (amphibolite and migmatite). The main rocks of the MGC are
118 metapelitic or metapsammitic migmatite and diatexite with subordinate centimeter- to meter-
119 scale bodies of granite (medium-grained two-mica granite to pegmatite) (Tomascak et al.
120 1996a, b). Migmatitic rocks commonly present well-distributed penetrative fabrics, interpreted
121 as deformation, which continued after migmatite formation and at subsolidus conditions
122 (Solar and Tomascak, 2016). An age of 376 ± 14 Ma has been obtained for migmatites from
123 the MGC (Solar and Tomascak, 2016). The MGC acts as country rock to the Sebago pluton,
124 located to the south. This pluton is quite homogeneous texturally and chemically, mainly
125 corresponding to a fine- to medium-grained, two-mica granite (Solar and Tomascak, 2016). It
126 is younger than the surrounding migmatites, with ages of 293 Ma (U-Pb TIMS in monazite,
127 Tomascak et al. 1996b). This important age difference between migmatites from the MGD
128 and the Sebago pluton rules out a direct relationship between both lithologies. According to
129 Solar and Tomascak (2009, 2016) migmatite-forming processes in this area had finished
130 before the formation of the Sebago pluton.

131 Pegmatites from the Oxford field present different degrees of evolution, from barren
132 bodies to highly evolved ones that show well-developed internal zoning (Roda-Robles et al.
133 2015b). They may intrude in migmatites, amphibolites and mica schists, either concordant to
134 the host rock foliation or as irregular and discordant bodies (Simmons et al. 2017). There is
135 not a general consensus on the origin of these pegmatites. According to Wise and Brown
136 (2010), they are related to the Sebago pluton by fractional crystallization processes.
137 However, pegmatites from this field have been dated in a range of ≈ 250 – 270 Ma (Bradley et
138 al. 2016), which means that they are >20 Ma younger than the Sebago pluton. This important
139 difference in the age of the two lithologies makes it difficult to link the origin of the pegmatites
140 to the Sebago pluton. More recent studies (Simmons et al. 2016; Webber et al. 2019)
141 propose a direct anatectic origin for these pegmatites, with the hosting migmatites and
142 metasedimentary rocks as the source for the pegmatitic melts.

143

144

GENERAL GEOLOGY OF THE BERRY-HAVEY PEGMATITE

145 The Berry-Havey pegmatite is a tabular to irregular body, hosted by a hornblende-rich
146 amphibolite, with minor diopside or biotite in places (Roda-Robles et al. 2015b). The lower
147 contact with the country rock is not observed, whereas the upper contact only outcrops to the
148 SW of the quarry. There, the pegmatite is mainly conformable to the country rock, dipping ~
149 40° SSE, whereas it gets more horizontal to the north (Fig. 2). Locally, the pegmatite
150 presents some thin (<50 cm thick) dike-like branches that intrude discordantly into the
151 country rock. No metasomatism effects have been observed in the hosting amphibolite close
152 to the contact with the pegmatite. According to the present level of exposure, the thickness of
153 the Berry-Havey pegmatitic body is estimated to be over 30 m. Nevertheless, the lack of
154 exposure of the footwall makes this estimation difficult. The pegmatite is cross-cut by three
155 sub-vertical mafic dykes with a NNE-SSW strike (Fig. 2). The Berry-Havey presents a well-
156 developed complex internal structure, where four different zones may be distinguished
157 according to their spatial distribution, textural features, paragenesis, and chemical
158 composition (Roda-Robles et al. 2015b) (Fig. 2; Table 1). These include a wall zone,
159 intermediate zone, core margin, and core zone. These zones are subparallel and may show
160 irregular limits among them, especially in the transition from the core margin to the core
161 zone. From the contact inward, the following units may be distinguished (Roda-Robles et al.
162 2015b) (Fig. 2; Table 1):

163 (1) The Wall Zone only outcrops at the SW area of the quarry, in direct contact with the
164 hosting amphibolite in the hanging wall. The wall zone most commonly presents a fine to
165 medium-sized pegmatitic texture. A gneissic texture may be locally observed. Main minerals
166 include quartz, plagioclase, K-feldspar, biotite, and muscovite, with tourmaline and garnet as
167 common minor phases, and accessory apatite.

168 (2) The Intermediate Zone volumetrically is the most important zone, as it corresponds to
169 ≈ 58 % of the outcrop. Its minerals include quartz and feldspars (K-feldspar and plagioclase)
170 which appear graphically intergrown in > 85 % of this zone. Other common phases are

171 biotite, muscovite, garnet, and black tourmaline, which occur scattered as fine- to medium-
172 sized crystals. Apatite occurs as an accessory phase. The intermediate zone appears over
173 and under the core zone/core margin. The upper intermediate zone is tabular, with a
174 thickness of ~5 m; whereas the lower intermediate zone, more important volumetrically, is
175 more irregular in shape and thickness (Fig. 2). To the N of the quarry the mineralogy and
176 texture of the lower intermediate zone change locally (Fig. 2). There mineralogy is simpler,
177 with quartz, K-feldspar and black tourmaline; whereas texturally the graphic intergrowth is not
178 observed and the grain size is coarser, locally with blocky K-feldspar and quartz, and with
179 black tourmaline prismatic crystals up to 40 cm in length.

180 (3) The Core Margin corresponds to $\approx 32\%$ of the pegmatite outcrop, occurring between
181 the upper and lower intermediate zone units, closer to the hanging wall than to the footwall
182 (Fig. 2). It is mainly composed of “vuggy” albite, quartz, muscovite, schorl, and accessory
183 green tourmaline and apatite. The lower limit between the core margin and the intermediate
184 zone is commonly marked by a discontinuous garnet-rich layer. This layer is used as a guide
185 for the miners in this region, as pockets are not usually found below this level. Over the
186 garnet layer, a quite continuous layer constituted by tourmaline prisms occurs in the core
187 margin (Fig. 2). The core margin zone envelops the different pods that constitute the core
188 zone of the pegmatite.

189 (4) The Core Zone is the innermost and most complex zone of the pegmatite. It is not a
190 continuous unit, but it is formed by a number of more or less irregular pods, sometimes
191 interconnected, of different sizes (from ≈ 2 m up to 10 m across) that are enclosed in the
192 core margin (Fig. 2). Main mineral phases of the core zone pods include blocky feldspars
193 and quartz, that host irregular masses of fine-grained, usually purple, lepidolite, book
194 muscovite \pm light pinkish lepidolite, albite, greenish and pinkish tourmaline, and sub-rounded
195 nodules of phosphates (with primary lithiophilite, triplite, dickinsonite, and/or montebasite);
196 with minor Cs-rich beryl and accessory cassiterite, Nb-Ta oxides and apatite.

197 (5) Pockets: the pods of the core zone may contain isolated or interconnected miarolitic
198 cavities (pockets), with very variable sizes, from a few cm^3 to $\approx 0.7 \text{ m}^3$. Two different mineral

199 associations may be observed inside these pockets. Some of them are Li-poor and may
200 include euhedral quartz crystals (often smoky), dark “etched” tourmaline, and zoned apatite
201 lenses. Most commonly, pockets are Li-rich, main minerals including quartz, blocky K-
202 feldspar, bladed albite, lepidolite, cassiterite, Cs-rich beryl, green and “watermelon” gemmy
203 tourmaline, and purple or bluish apatite. In addition, in both the core margin and the core
204 zone, locally some elongated “seams” of ≤ 50 cm long and ≤ 20 cm wide, which may be filled
205 with apatite, can be observed. These seams are hosted by blocky feldspar in the core zone
206 and/or by platy albite in the core margin.

207 **Textural features of the apatite**

208 Apatite is ubiquitous in all the units distinguished in the Berry-Havey pegmatite although
209 in different proportions. In the wall zone and intermediate zone, apatite is an accessory
210 phase, appearing as grayish, fine-grained anhedral to euhedral crystals (< 5 mm) (Table 1,
211 Fig. 3a). It is more abundant in the core margin, occurring as fine to medium-sized (< 3 cm),
212 bluish prismatic to anhedral crystals. In addition, some anhedral crystals occur intergrown
213 with garnet in the garnet layer, between the intermediate zone and the core margin (Fig. 3b).
214 In the core zone apatite is very scarce in the pods, where it occurs as subhedral to euhedral
215 fine-grained prisms (< 3 mm) showing concentric zoning under the petrographic microscope
216 (Fig. 3c). In contrast, apatite is abundant in many of the pockets, where it can even be the
217 main phase in the seams, which can be filled up with strongly colored apatite (Fig. 3d). In
218 general, apatite from the pockets is subhedral to euhedral, often occurring as short
219 hexagonal prisms or lenses (< 1 cm \varnothing) with different colors in hand sample. In the Li-poor
220 pockets euhedral apatite crystals coat or grow over euhedral quartz crystals (Fig. 3e), also
221 coexisting with etched dark tourmaline. These euhedral crystals correspond to hexagonal
222 lenses that show concentric sharp zoning, with a grayish to clear blue core and a narrow
223 pure whitish rim (Fig. 3e). In Li-rich pockets, apatite short prisms show a deep purple or
224 bluish color without concentric chromatic zoning (Fig. 3f). The anhedral to prismatic apatite
225 that fills the elongated “seams” also presents a common deep purple color (Fig. 3d).
226 Occasionally, it is also possible to observe in those cavities some euhedral short hexagonal
227 apatite prisms that present a purple core and a deep green rim.

228

229

SAMPLING AND ANALYTICAL METHODS

230 Apatite samples were taken from all the zones of the pegmatite. Those from the core
231 zone, where apatite is especially abundant in some of the pockets and in some elongated
232 “seams”, are the best-represented samples. Characterization of apatite was carried out via
233 the study of its texture in hand sample and thin section, and of its chemical composition by
234 electron-microprobe and LA-ICP-MS techniques.

235 Electron-microprobe quantitative analyses were performed at the University of Paul
236 Sabatier (Toulouse, France) using a Cameca SXFive (Raimond Castaing Center). The
237 operating conditions included an accelerating voltage of 15 kV; a beam current of 10 nA, and
238 a beam diameter of 2 μm . A low current was used due to the sensitivity of apatite under the
239 beam. Analyzed surfaces were chosen in the same way to reduce damage. The time of
240 analyses was 10s for each element and 5s on the background; except for F, with 20s and
241 10s on the background. The following standards were used: albite (Na), periclase (Mg),
242 corundum (Al), wollastonite (Ca, Si), hematite (Fe), MnTiO_3 (Mn), tugtupite (Cl), Durango
243 apatite (F, P), LaPO_4 (La), CePO_4 (Ce), and celestine (Sr). Data were reduced using the
244 procedure of Pouchou and Pichoir (1985). Analytical errors are estimated to be on the order
245 of $\pm 1\text{--}2\%$. Measuring of F and Cl by EMPA may involve difficulties that may be solved by
246 doing the analyses having crystals oriented with their *c*-axes perpendicular to the incident
247 electron beam (Goldoff et al. 2012). In the present study only analyses made on the apatite
248 crystals from the Li-poor, Li-rich pockets and seams could be oriented this way.

249 Trace element analyses in apatite were performed by laser-ablation inductively-coupled
250 plasma mass-spectrometry (LA-ICP-MS) at the Geochronology and Isotope Geochemistry-
251 SGIker facility of the University of the Basque Country (Spain). More than 100 analyses were
252 performed by the ablation of apatite crystals in ca. 100 μm thick petrographic sections or on
253 crystals mounted in epoxy using a UP213 Nd:YAG laser ablation system (New Wave)
254 coupled to a Thermo Fisher Scientific X Series 2 quadrupole ICP-MS instrument with
255 sensitivity enhanced through a dual pumping system. Spot diameters of ca. 100 μm were

256 used for analyses, associated with repetition rates of 10 Hz and laser fluence at the target of
257 ca. 5.5 J/cm². The ablated material was carried in He and then mixed with Ar. The NIST SRM
258 612 reference glass was used to perform tuning and mass calibration, by inspecting the
259 signal of ²³⁸U to obtain ca. 14,000,000 cps/ppm, and by minimizing the ThO⁺/Th⁺ ratio to
260 ca. 1%. Raw data were processed using Lolite 2.3 (Paton et al. 2011; Paul et al. 2012) and
261 Ca as an internal standard (data obtained by electron microprobe). Apatite from Cerro
262 Mercado (Durango, Mexico) was used to optimize the procedure and as a secondary
263 standard to control the quality of the results in each analytical session.

264

265 **APATITE MINERAL CHEMISTRY**

266 **Major elements**

267 Apatite from the Berry-Havey pegmatite presents chemical differences for some major
268 elements depending on the unit where it occurs (Table 2, Fig. 4). In addition, some crystals
269 show marked concentric zoning for certain elements. All the analyzed apatite crystals are
270 fluorapatite. The highest F contents correspond to apatite from the pockets, with values
271 ranging from 5 to 6.14 wt% for the purple prisms, 4.99 to 5.91 wt% for the zoned gray-white
272 lenses, and 2.96 to 3.81 wt% for the zoned purple-green crystals of the seams (Table 2, Fig.
273 4a). The F content of apatite from the intermediate zone is as well > 4 wt%. Wall zone apatite
274 has 2.84 to 3.10 wt% F. The lowest F values correspond to apatite from the core margin, in
275 the range 1.28 – 2.98 wt% F (Table 2, Fig. 4a). The OH content in the halogen site is low in
276 general, ranging from 0 apfu in the apatite from the intermediate zone, Li-poor and Li-rich
277 pockets; up to > 0.5 apfu in the apatite from the core margin; with intermediate values in
278 apatite from the wall zone, seams, and core zone pods (Table 2). All the analyzed apatite
279 crystals have extremely low Cl contents, the highest value (0.13 wt%) corresponding to a
280 zoned gray-white crystal from a pocket (Table 2).

281 The most significant differences for the major elements on the pegmatite and single
282 crystal scales correspond to Mn (Table 2, Figs. 4b, 5a,b, 6a). The lowest Mn values are
283 found in apatite from the wall zone (0.07-0.20 wt% MnO), from the pods of the core zone

284 (0.06-0.55 wt% MnO), and in the purple crystals from the Li-rich pockets (0.08-0.48 wt%
285 MnO). In contrast, apatite crystals from the Intermediate zone and core margin show higher
286 Mn values in the range of 3.10-9.97 wt% MnO. Zoned gray-white apatite crystals from the Li-
287 poor pockets present marked Mn variations across the crystals, from 4.65 wt% MnO in the
288 grayish cores to 0.21 wt% MnO in the white rims (Table 2, Fig. 6a). In the case of the purple-
289 green crystals from the seams, the variation trend is not so clear but, overall, Mn values
290 increase from the purple core (0.93-3.26 wt% MnO) to the greenish rim (3.67-4.23 wt% MnO)
291 (Fig. 6a).

292 Iron contents are low in all the analyzed apatite, i.e. always ≤ 0.32 wt% FeO (Table 2,
293 Figs. 5b, c). A clear relation between the pegmatite unit and the Fe content has not been
294 determined. However, a certain positive correlation between the Mn and Fe contents is
295 observed (Fig. 5b). In the case of the zoned crystals, in the gray-white lenses there is a slight
296 Fe decrease from core (0.31 wt% FeO) to rim (0.00 wt% FeO) (Fig. 6b). In contrast, like Mn,
297 in the purple-green zoned crystals the Fe tends to increase from the purple core (0.07-0.15
298 wt% FeO) to the greenish rim (0.17-0.18 wt% FeO) (Fig. 6b).

299 Calcium values also show some differences. In general, as expected, there is a good
300 negative correlation between Ca and Mn (Figs. 4c, 5a, 6a, c), with the lowest contents
301 (41.72-43.39 wt% CaO) in the Mn-richest crystals from the core margin, and the highest Ca
302 contents (55.00 to 55.99 wt% CaO) in the Mn-poorest apatite from the wall zone and the core
303 zone. Although it may display a clear chromatic concentric zoning under the microscope (Fig.
304 3c), no chemical zoning of major elements has been observed in apatite crystals from the
305 core zone pods.

306

307 **Trace elements**

308 Like major elements, some trace elements in apatite show differences depending on the
309 pegmatitic unit and across zoned crystals. Main variations correspond to REE, Y, and Sr
310 (Fig. 7a-e). Yttrium and REE show similar trends, with a continuous decrease from the wall
311 zone to the core zone (Table 3, Figs. 7a-d, 8a). Values for Y and Σ REE for apatite from the
312 wall zone are in the ranges 1155 to 1503 ppm and 1796 to 2178 ppm, respectively. In the

313 intermediate zone, these values decrease to 225 to 261 ppm Y and 1219 to 1280 ppm
314 Σ REE. Apatite from the core margin is even poorer, with values of 22.7 to 26.3 ppm Y and
315 309 to 355 ppm Σ REE. In the core zone, there are significant differences in the Y and Σ REE
316 contents when comparing apatite from the pods and that of the different types of pockets.
317 Apatite from the pods is the poorest in these elements, with Y contents below the detection
318 limit and Σ REE values < 0.14 ppm (Table 3, Figs. 7, 8a). Purple apatite of the Li-rich pockets
319 also shows extremely low contents of Y (0.14-0.54 ppm) and Σ REE (0.11-0.37 ppm). Zoned
320 gray-white apatite crystals from the Li-poor pockets are richer in these elements, with Y and
321 Σ REE values varying respectively in the range of 979 to 31.7 ppm, and 921 to 41.3 ppm from
322 grayish core to white rim (Table 3, Figs. 7b, c, d, 8a, b, 9a-d). The zoned purple-green
323 apatite from the seams has intermediate Y and Σ REE values, with Y and Σ REE contents that
324 vary respectively in the ranges of 2 to 23 ppm and 0 to 5 ppm, and 53.2 to 210 ppm and 0.0
325 to 42.2, for the purple cores and greenish rims, respectively (Table 3, Figs. 7a-d, 8a, b, c, 9a-
326 d).

327 Overall, Sr presents a more complex trend, with a rough negative correlation with Σ REE
328 and Y (Figs. 7a, b, e, 8b, c; 9e). On the pegmatite scale, there is a Sr decrease in apatite
329 from the wall zone to the intermediate zone, and a final marked increase in the pods of the
330 core zone and pockets (wall zone: 50-52.5 ppm; intermediate zone: 2.9-16.1; core margin:
331 2.6-23.4 ppm; core zone pods: 18-1614; Li-poor pockets: 507-28710 ppm; Li-rich pockets:
332 5910-19800 ppm; seams: 17-3640 ppm) (Table 3, Figs. 7e, 8b, c). Apatite from the pods of
333 the core zone, as well as the zoned crystals from the Li-poor pockets and seams (gray-white
334 and purple-green respectively), show significant Sr variations on the crystal scale (Table 3,
335 Fig. 9e). The greatest variations correspond to the gray-white apatite crystals, where the Sr
336 content changes in the range from 759 ppm in the core to 28710 ppm in the rim, with a
337 continuous increase outwards (Fig. 9e). The Sr content of the purple-green zoned crystals
338 from the seams also increases outwards, from 17 to 207 ppm Sr in the purple core to 93 to
339 3640 ppm in the green rim (Table 3, Fig. 9e). Some of the small euhedral apatite crystals
340 from the core zone pods (Fig. 3c) also present an increasing Sr-trend from the core (27 ppm)
341 to rim (662 ppm) (Table 3).

342 Uranium, Th, and Pb concentrations also show differences on the pegmatite and mineral
343 scales (Table 3, Figs. 7f, g, h, 8d, e, f). Uranium values are higher than the Pb contents in
344 apatite from the wall zone, intermediate zone, and core margin. Thorium is only higher than
345 Pb in apatite from the intermediate zone and core margin (Fig. 8d, e). Likewise, the rims of
346 gray-white zoned crystals from the Li-poor pockets and those of zoned crystals from the core
347 zone pods are richer in U than in Pb. The highest U and Th contents correspond to apatite
348 from the core margin (153-590 ppm U and 154-190 ppm Th), whereas the lowest contents
349 are those from the purple crystals from the Li-rich pockets (0.04-0.82 ppm U and Th below
350 detection limits) and from the pods of the core zone (0.01-49.2 ppm U and <0.2 ppm Th)
351 (Table 3, Figs. 7f, g, h, 8d, e, f). On the crystal scale, U, Pb, and Th elements behave
352 similarly in the purple-green crystals, with an initial increase and a later decrease from core
353 to rim (Fig. 9f, g, h); whereas in the gray-white crystals, Pb and Th behave similarly, with a
354 decrease from the core to the rim, whereas U presents the opposite trend (Fig. 9f, g, h).

355 The pairs of elements Y-Ho and, to a lesser extent, Zr-Hf show good positive
356 correlations (Fig. 8g, h). There is a continuous decrease in the Y and Ho contents from the
357 wall zone, through the intermediate zone, followed by the core margin and the core zone. On
358 the crystal scale, the gray-white and purple-green zoned crystals show a clear depletion in Y
359 and Ho from the core to the rim (Fig. 9a, b, d), whereas in apatite from the core zone pods
360 their content is below the LA-ICP-MS detection limit. In contrast to Y-Ho, a clear relationship
361 between pegmatite units and Zr-Hf contents has not been identified. The highest contents in
362 both elements correspond to the zoned apatite crystals from the core zone pods and to the
363 rims of the purple-green prisms from the seams (Fig. 8h).

364

365 **REE patterns**

366 Chondrite-normalized REE patterns for apatite from different zones of the pegmatite
367 show significant differences, with a continuous decrease inwards. The wall zone apatite
368 crystals present nearly sub-horizontal well-defined patterns, a marked negative Eu anomaly
369 (0.08-0.09) and slight tetrad effects (Figs. 10a, 11). Apatite from the intermediate zone is
370 poorer in REE and shows a quite different pattern, with a pronounced negative slope for the

371 HREE, very marked Eu negative anomaly (0.01-0.02) and strong tetrad effects (Figs. 10a,
372 11). The lanthanide pattern for apatite from the core margin is similar to that of the
373 intermediate zone, but with lower concentrations. It also presents a marked negative slope
374 for the HREE, strong but less marked Eu negative anomaly (0.12-0.15), and important tetrad
375 effects (Figs. 10a, 11). Apatite of pods in the core zone is extremely impoverished in REE,
376 with no or incomplete/erratic patterns. This is also the case for the purple apatite crystals
377 from the Li-rich pockets (Figs. 10a, 11).

378 The zoned apatite crystals from the Li-poor pockets and seams show significant
379 variations in their lanthanide patterns with an overall decrease from core to rim. The patterns
380 for the gray-white crystals are well-defined. The core and intermediate areas of the crystals
381 show sub-horizontal patterns, whereas in the rims the patterns slope upwards from LREE to
382 HREE (Fig. 10b). The Eu negative anomaly decreases from core to rim (Figs. 10b, 11). In the
383 whole crystals, the tetrad effects are equally important, but less pronounced than in apatite
384 from the intermediate zone and core margin (Figs. 10b, 11).

385 The purple-green zoned crystals in the seams also show conspicuous lanthanide zoning.
386 As in the gray-white lenses, the REE contents decrease outwards, in tandem with a
387 decrease in the Eu anomaly. However, in contrast with the gray-white lenses, the Eu
388 anomaly becomes positive in many rim analyses (0.52-2.97). The patterns tend to slope
389 downwards from LREE to HREE and the tetrad effects are less pronounced (Figs. 10c, d,
390 11).

391

392

DISCUSSION

393 Variations in Mn

394 The analyzed apatite crystals from the Berry-Havey pegmatite show a negative Ca-Mn
395 correlation (Fig. 5a), with the highest Mn values in apatite from the core margin and
396 intermediate zone, and the lowest in the wall zone and core zone (Fig. 4). According to some
397 authors (e.g. Miles et al. 2013; Belousova et al. 2002), reducing conditions could favor the
398 incorporation of Mn in apatite as the size (0.66Å) and charge of Mn²⁺ are more similar to
399 those of Ca²⁺ (1.00Å) than those of Mn³⁺ (0.58Å) and Mn⁴⁺ (0.39Å). The evolution of the *f*O₂

400 during pegmatitic crystallization is usually difficult to determine. The composition of biotite
401 from the wall zone and intermediate zone (unpublished data) is consistent with the NNO
402 buffer (calculated according to the diagram of Wones and Eugster, 1965). Also, the presence
403 of $(\text{Fe}+\text{Mn})^{2+}$ -rich primary phosphates such as lithiophilite ($\text{LiMn}^{2+}\text{PO}_4$), triplite ($\text{Mn}^{2+}_2(\text{PO}_4)\text{F}$)
404 and dickinsonite ($(\text{KNa})(\text{Mn}^{2+}\square)\text{Ca}(\text{Na}_2\text{Na})\text{Mn}^{2+}_{13}\text{Al}(\text{PO}_4)_{11}(\text{PO}_4)(\text{OH})_2$) in the pods of the core
405 zone indicates that the $f\text{O}_2$ was still reduced to predominantly Fe^{2+} near NNO (London, pers.
406 comm) at least until the beginning of the crystallization of the core zone. In contrast, the
407 chemical composition of Li-tourmaline (elbaite-darrellhenryite) coexisting with purple apatite
408 in the Li-rich pockets from the core zone reveals a final increase in the $f\text{O}_2$ that enables the
409 elbaite-darrellhenryite exchange vector ($^{\text{Y}}\text{Al}^{\text{W}}\text{O}_2^{\text{Y}}\text{Li}_{-1}^{\text{W}}(\text{OH})_{-2}$) to operate during the
410 crystallization of the gemmy tourmaline found in the Li-rich pockets (Roda-Robles et al.
411 2015b). Moreover, the Eu and Ce anomalies observed in apatite from the pockets mainly
412 correspond to oxidizing conditions (see below). Accordingly, redox conditions during the wall
413 zone, intermediate zone, and core margin crystallization were likely reduced, shifting toward
414 more oxidizing conditions during the crystallization of the core zone pods. Finally, the
415 pockets most probably crystallized under oxidizing conditions (Fig. 12a). Thus, the
416 incorporation of Mn into apatite of the intermediate zone and core margin could have been
417 favored by the relatively low $f\text{O}_2$ of the pegmatitic melt, near the NNO buffer. However,
418 factors other than redox conditions should have contributed to the high Mn content in apatite
419 of some pockets, as well as to the low Mn content in apatite of the wall zone. Even though
420 crystallization of the wall zone most probably proceeded under low $f\text{O}_2$ conditions, the Mn
421 content in apatite from this zone is very low. The most feasible reason may be related to low
422 availability of Mn in the pegmatitic melt at the beginning of crystallization. This would be
423 supported by the garnet chemistry in the wall zone, which corresponds to almandine
424 ($\text{Alm}_{76.2}\text{Sp}_{19.5}\text{Pyr}_{4.3}$, Roda-Robles et al. 2017). The spessartine component increases from
425 core to rims in single garnet crystals and from the wall zone up to the core margin as a result
426 of fractionation (Roda-Robles et al. 2017), a behavior commonly observed in many
427 pegmatites (e.g. Baldwin and von Knorring, 1983; Černý et al. 1985; Sokolov and Khlestov,
428 1990; Hernández-Filiberto et al. 2021). Therefore, at the beginning of pegmatite

429 crystallization, Mn concentration in the melt would be relatively low, which is reflected not
430 only in the garnet but also in the apatite composition of the wall zone.

431 In contrast, the highest Mn values in apatite are found in the core margin. Garnet
432 coexisting with this apatite corresponds to spessartine ($\text{Alm}_{42.6}\text{Sp}_{57.3}\text{Pyr}_{0.1}$, Roda-Robles, et
433 al. 2017), which means a higher availability of Mn in the melt during the formation of core
434 margin than during the formation of wall zone. The previous crystallization in the wall zone
435 and intermediate zone of tourmaline (schorl/foitite) and, to a lesser extent, biotite would allow
436 the MnO/FeO ratio of the pegmatitic melt to increase, as Mn is incompatible or presents a
437 low compatibility with these two minerals (London et al. 2001a; García-Serrano et al. 2017;
438 Maner et al. 2019).

439 The Mn content of apatite in pods of the core zone becomes low again (Figs. 4a, 5a),
440 even though the fO_2 was still reduced during their crystallization (as supported by the
441 presence of nodules of Mn^{2+} -rich primary phosphates). An explanation for this Mn depletion
442 in apatite may be found in the consumption of most of the Mn by these Mn-rich phosphate
443 nodules in the core zone pods, which would drastically reduce the concentration of Mn in the
444 remaining melt.

445 Finally, apatite from the pockets and seams shows important differences in the Mn
446 contents, which may account for different time/conditions in the formation of miarolitic
447 cavities, even if they are found in relatively close proximity to other cavities, mainly in the
448 core zone. Like the apatite from core zone pods, the purple apatite of Li-rich pockets inside
449 those pods is Mn-poor. Miarolitic cavities usually are found in the innermost part of zoned
450 pegmatites and are considered to represent the transition from an igneous to a hydrothermal
451 stage, hosting minerals that first formed from a silicate melt and, later, others that crystallized
452 from an aqueous solution (Jahns, 1982; London et al. 2020). Actually, the temperatures
453 estimated for pocket formation are relatively low, in the range of 435-355°C (London et al.
454 2020). In the case of the Berry-Havey pegmatites, the pegmatite crystallized from the
455 borders inwards and, according to the mineralogical association, mineral chemistry, and
456 spatial distribution, the Li-rich pockets were formed during the latest crystallization stages, at
457 the lowest temperatures and most oxidizing conditions (Roda-Robles et al. 2015b). There are

458 several lines of evidences to support this. First, these pockets are usually hosted by the most
459 fractionated pods of the core zone, with significant amounts of Li-F±B±P-rich phases (e.g.
460 lepidolite, F-elbaite, montebrasite (LiAl(PO₄)(OH, F)) and lithiophilite). The K/Rb ratio in K-
461 feldspar and mica, which has been often used as an indicator of the fractionation degree of
462 granitic pegmatites (e.g. Roda-Robles et al. 2006; London et al. 2012; Brown et al. 2017;
463 Garate-Olave et al. 2018), decreases progressively from the wall zone (308-425 in K-feldspar
464 and 116-125 in Al-mica), through the intermediate zone (98-131 in K-feldspar and 41-101 in
465 Al-mica) and the core margin (10-44 in Al-mica), to the core zone, where this ratio is as low
466 as 15 to 20 for K-feldspar and 6 to 18 for Al-mica (unpublished data). Moreover, the Li
467 content in tourmaline (Roda-Robles et al. 2015b) and in mica increases along the same path.
468 The inward increase in the F content from the beginning of crystallization is evidenced by the
469 Fluorine Intercept Value in biotite, calculated according to Munoz (1984), which decreases
470 from 4.22 in the wall zone, to 3.91 in the intermediate zone below the core margin, and to 3.5
471 in the intermediate zone over the core margin. An even higher F-content in the melt at the
472 final crystallization stages is attested by the common occurrence of the F-rich tourmaline in
473 the core margin and core zone (Roda-Robles et al. 2015b) as well as by the presence of
474 subrounded montebrasite pods in the core zone with F values in the range 3.1-5.6 wt%
475 (unpublished data). According to the correlation between F in montebrasite and F in the melt
476 determined by London et al. (2001b), the [F] in the melt during the core zone crystallization
477 would be in the range 0.83-1.51 wt%. Therefore, the Li-rich pockets would have formed at
478 the latest stages of crystallization of the Berry-Havey pegmatite and, by then, most of the Mn
479 could have been consumed. This, in conjunction with the high fO_2 and high concentration of
480 fluxes, arguably contributed to the low Mn content in the purple apatite of the Li-rich pockets.

481

482 **Strontium and Y variations**

483 Opposite to Mn and some REE (see below), the Sr and Y contents in apatite are
484 believed to be independent of the fO_2 (Yu et al. 2021). Feldspars can accommodate Sr
485 substituting for Ca and/or K (Smith, 1974), and its compatible behavior causes its
486 concentration to typically decrease in apatite with fractionation (e.g., Belousova et al. 2002;

487 Chu et al. 2009; Cao et al. 2012; 2013; Pan et al. 2016; Azadbakht et al. 2018).
488 Consequently, apatite associated with fractionated granites and pegmatites often has the
489 lowest Sr values, in some cases < 100 ppm (Belousova et al, 2002). In the Berry-Havey
490 pegmatite, in the first stages of crystallization Sr behaves accordingly, its content in apatite
491 decreasing from the wall zone to the intermediate zone. However, the Sr trend exhibits an
492 inflection point in the intermediate zone, and apatite becomes richer from the intermediate
493 zone, through the core margin, to the core zone, with the highest Sr-contents in apatite from
494 pockets and seams, sometimes close to 3 wt% (Figs. 7e, 8b, c; Table 3). Similar behavior
495 has been recently described and discussed in apatite occurring in the most fractionated
496 pegmatites and leucogranites from the Central Iberian Zone (Spain and Portugal) (Roda-
497 Robles et al. 2022). In the Berry-Havey pegmatite, plagioclase composition changes
498 progressively from the contact with the country rock inward, with a dramatic decrease in the
499 CaO and Sr contents from the wall zone (up to 13 wt% and 1044 ppm, respectively) to the
500 intermediate zone (< 1.14 wt% and < 4 ppm, respectively), and even lower in plagioclase
501 from the core margin and the core zone (< 0.1 wt% and < 2 ppm, respectively) (unpublished
502 data). According to the experimental works of Icenhower and London (1996), and the data
503 compiled by Smith (1974), plagioclase with an Na content corresponding to the andesine
504 composition may be richer in Sr than other more anorthitic feldspars. However, chemical
505 variations observed in plagioclase from the Berry-Havey pegmatite clearly indicate that the
506 most albitic plagioclase is the poorest in Sr, as may also be seen in the data compiled by
507 Smith (1974) for pegmatitic feldspars. Accordingly, we propose that the extremely Na-rich
508 composition of plagioclase from the high levels of magmatic fractionation could have made it
509 difficult for Sr to enter into the structure of the very pure albite. Consequently, Sr could have
510 started behaving as an incompatible element from the crystallization of the intermediate
511 zone, with the concomitant Sr increase in apatite from the inner zones of the pegmatite,
512 which at that point would have been the only sink for Sr in that highly evolved paragenesis.
513 This increasing trend for Sr is also observed in the individual zoned crystals, with Sr poorer
514 cores and richer rims (Fig. 9e). This is especially observed in gray-white lenses, whose Sr-

515 values in the rims (19,800-28,710 ppm) are nearly 40 times higher than those of the cores
516 (507-759 ppm).

517 Yttrium behavior in apatite is commonly opposite to that of Sr. The Y-richest apatite (>1
518 wt%) is associated with granitic pegmatites (Belousova et al. 2002), as this element usually
519 behaves as incompatible, increasing with magmatic fractionation (e.g., Belousova et al.
520 2002; Chu et al. 2009; Cao et al. 2012; Bromiley, 2021). However, like the REE, Y tends to
521 decrease in LCT granitic pegmatites (those enriched in Li, Cs and Ta) with fractionation. This
522 could be related to the relatively high availability of P in these pegmatitic melts, as attested to
523 by the common occurrence of phosphates in these rocks. Under such conditions, early
524 crystallization of Y(+REE)-bearing phosphates, such as xenotime-Y and/or monazite-Ce,
525 even in very low proportions, may lead Y and REE to behave as compatible, hence depleting
526 their concentration in melts during fractionation (Jolliff et al. 1989). In the Berry-Havey
527 pegmatite, Fe-Mn- and Al-phosphates are common in the inner zone, which indicates that P
528 concentration in the melt was high enough to attain phosphate saturation. Monazite-Ce and
529 xenotime-Y are accessory minerals that are found in the intermediate zone and in the garnet
530 layer between the intermediate zone and the core margin. Therefore, it would be possible
531 that early crystallization of these phases could be responsible for the Y and REE depletion in
532 apatite during fractionation of the Berry-Havey pegmatite, with a decrease for apatite from
533 the wall zone, through the intermediate zone and the core margin; up to the core zone.
534 Zoned apatite crystals also show a decreasing Y-content from core to rim (Fig. 9d).

535

536 **REE patterns**

537 At the Berry-Havey pegmatite, the REE content in apatite decreases from the wall zone
538 inwards, i.e., with magmatic evolution, as it has been previously reported in other localities
539 (e.g., Jolliff et al. 1989; Bromiley, 2021; Roda-Robles et al. 2022). Incorporation of REE into
540 apatite occurs via two main substitution mechanisms that mainly involve Ca and, to a lesser
541 extent, P, Si and Na: $\text{REE}^{3+}_1\text{Na}^+_1\text{Ca}^{2+}_{-2}$ and $\text{REE}^{3+}_1\text{Si}^{4+}_1\text{P}^{5+}_{-1}\text{Ca}^{2+}_{-1}$ (Sha and Chapell, 1999;
542 Pan and Fleet, 2002; Webster and Piccoli, 2015; Harlov, 2015). The low REE content in the

543 studied apatite impedes the determination of the influence of the two exchange vectors in the
544 incorporation of REE in the studied apatites.

545 Nearly all the studied apatite crystals show more or less pronounced tetrad effects, with
546 values of $TE_{1,3} > 1.1$ (calculated according to Irber, 1999). Except for apatite from the wall
547 zone that presents intermediate $TE_{1,3}$ values, the tetrad effects become less marked in
548 apatite from intermediate zone to core zone, parallel to a decrease in the Y content. (Fig.
549 11b). According to some authors, strong tetrad effects in apatite may be related to high fluid
550 activity in the melt (Kawabe, 1995; Bau, 1996; Irber, 1999; Monecke et al. 2002; Zhao et al.
551 2002). However, aqueous fluid activity in the pegmatitic melt during the crystallization of the
552 inner zones of the Berry-Havey pegmatite (core margin, core zone) would probably be much
553 higher than during the crystallization of the intermediate zone. Even more so, apatite crystals
554 associated with the pockets, which are likely related to the activity of aqueous fluids exsolved
555 from the pegmatitic melt, have much lower $TE_{1,3}$ values than apatite from the intermediate
556 zone, the core margin and, in some cases, the wall zone. Consequently, tetrad effects in the
557 apatite from the Berry-Havey pegmatite appear to be unrelated to the aqueous fluid activity
558 during their crystallization.

559 The abundance of aqueous fluids has also been proposed to be associated with non-
560 CHARAC (CHARGE-and-RADIUS-CONTROLLED) Y/Ho ratios (Bau, 1996; Peretyazhko and Savina,
561 2010; Cao et al. 2013). Most of the studied apatite crystals from the Berry-Havey pegmatite
562 plot out of the Y/Ho CHARAC range (24-34) (Fig. 12b). Only Y/Ho ratios from apatite from
563 the wall zone and some values corresponding to the purple cores of zoned crystals from the
564 seams plot in or close to those values. It should be noted that Y/Ho values increase
565 progressively for apatite from the wall zone, the intermediate zone, and the core margin.
566 Similarly, in the zoned crystals from the pockets and seams, the Y/Ho value increases
567 outwards, i.e. during crystallization. Purple apatite from the Li-bearing pockets also shows
568 some of the highest Y/Ho values. In short, the apatite of the Berry-Havey pegmatite shows a
569 non-CHARAC behavior that is characteristic of magmatic-pegmatitic systems with high SiO_2
570 contents enriched in H_2O , Li, B, F, P, and/or Cl, as suggested by Bau, (1996); Peretyazhko
571 and Savina, (2010) and Cao et al. (2013).

572

573 **Europium and Ce anomalies**

574 Most of the REE present just a single trivalent valence state and are readily incorporated
575 into apatite via the two REE coupled substitutions noted above. In contrast, Eu and Ce may
576 occur with two different oxidation states (Eu^{2+} - Eu^{3+} and Ce^{3+} - Ce^{4+} , respectively) (e.g.,
577 Burnham and Berry, 2014). In both cases, the trivalent Eu and Ce cations are more easily
578 incorporated into the apatite structure thanks to the higher similarity of their ionic size to that
579 of Ca^{2+} (Cao et al. 2013). As a result, Eu and Ce can present anomalous contents in apatite
580 compared to the other trivalent REE (Bromiley, 2021). Such anomalies have been often
581 related to $f\text{O}_2$ conditions during the crystallization of melts, with strong Eu-negative
582 anomalies (high $\text{Eu}^{2+}/\text{Eu}^{3+}$ ratios) in apatite formed under low $f\text{O}_2$, and no or positive Eu
583 anomalies under relatively oxidizing conditions (e.g. Sha and Chappell, 1999; Pan and Fleet,
584 2002; Belousova et al. 2002; Chu et al. 2009; Cao et al. 2012; Miles et al. 2014; Azadbakht
585 et al. 2018; Bromiley, 2021). In addition, the Eu anomaly may be conditioned by the
586 crystallization of other mineral phases that compete for this element, namely feldspars,
587 where Eu^{2+} is highly compatible (especially in K-feldspar) (Kontak and Martin, 1997;
588 Belousova et al. 2002). Consequently, if apatite crystallizes after or during the formation of
589 feldspar, it would show a negative Eu anomaly (Drake and Weill 1975; Sha and Chappell,
590 1999; Belousova et al. 2002; Cao et al. 2013; Miles et al. 2014; Abdullin et al. 2016). The Ce
591 anomaly is usually less pronounced than the Eu anomaly (Sha and Chappell, 1999;
592 Belousova et al. 2002; Chu et al. 2009; Ding et al. 2015), and it does not seem to be affected
593 by the presence of other minerals except for the REE-bearing phases such as zircon,
594 monazite, or xenotime. (Bromiley, 2021). Compared to the Eu anomaly, the Ce anomaly is
595 considered to be less appropriate to assess the redox conditions during apatite crystallization
596 (Cao et al. 2012), but a combination of both anomalies seems to be more useful for that
597 purpose (Cao et al. 2012; Pan et al. 2016; Azadbakht et al. 2018).

598 Apatite from the Berry-Havey pegmatite presents significant differences in Eu and Ce
599 anomalies regarding its position inside the body, with a negative correlation for both values
600 (Fig. 12b). The strongest Eu negative and Ce positive anomalies correspond to apatite of the

601 intermediate zone, which suggests reducing conditions and would be in agreement with the
602 high Mn contents of apatite from this zone. However, the abundance of feldspars in the
603 intermediate zone (> 85 vol%) could also have influenced the availability of Eu for the
604 coexisting apatite, enhancing its negative Eu anomaly in the intermediate zone. On the other
605 hand, the less marked Eu and Ce anomalies in the wall zone apatite compared to the
606 intermediate zone (Fig. 12a) could be related to the early character of this phosphate in the
607 wall zone, inferred from textural characteristics (Fig. 3a). In the core margin the apatite
608 presents a less marked Eu anomaly, plotting in the “moderate oxidized” field (Fig. 12b),
609 which is in agreement with an increase of fO_2 inwards during pegmatite crystallization.
610 Moreover, except for garnet, no other phases competing for Eu coexist with apatite in this
611 zone. The garnet intergrown with bluish apatite in the core margin (Fig. 3b) is extremely
612 depleted in REE, which shows an erratic pattern (unpublished data). This indicates that
613 apatite controls the lanthanide distribution in the core margin. The extremely low REE
614 concentration in apatite from the core zone pods and the Li-rich pockets prohibits evaluation
615 of their Eu or Ce anomalies.

616 The zoned apatite crystals from the Li-poor pockets and seams show significant
617 differences from core to rim. In the first case, all the values plot in the “moderate oxidized”
618 field (Fig. 12a). The decrease in Eu and Ce anomalies from the gray core to the whitish rim
619 could well correspond to an increasing fO_2 during crystallization of the Li-poor pockets, as it
620 is also supported by the progressive decrease in Mn from core to rim in those lenses. Zoned
621 apatite crystals from the seams present a much broader range for the Eu anomaly than that
622 of Ce. While the purple cores of these crystals plot mainly in the “moderate oxidized” field,
623 many of the greenish rims show a positive Eu anomaly falling in the “oxidized” field (Fig.
624 12a). Accordingly, the fO_2 could have increased dramatically during crystallization of the
625 seams. Nevertheless, lower or positive Eu anomalies in apatite from the pockets and the
626 seams could also be related to the higher solubility of Eu in F- and Cl-rich H_2O -fluids
627 exsolved from the melt, in comparison with the other REEs (Abramov, 2001).

628

629 **Chemistry of apatite as a recorder of the crystallization history of the Berry-Havey**
630 **pegmatite**

631 Evidence for the exsolution of H₂O-rich fluids during the last stages of crystallization of
632 the Berry-Havey pegmatite is supported by the occurrence of pockets in the innermost parts
633 of the body. Based on the apatite composition and the mineral association of the different
634 types of pockets (Li-rich, Li-poor, and seams), the exsolution of fluids presumably proceeded
635 during different crystallization stages with, at least, three generations of pockets. The earliest
636 one would correspond to the Li-poor pockets where gray-white zoned apatite lenses occur.
637 Exsolution of the fluids would take place at the end of the crystallization of the core margin,
638 when the availability of Fe, Mn, and REE was still high enough for the crystallization of Fe-
639 rich tourmaline (schorl) and Mn+REE-rich apatite. Exsolution processes could be related to a
640 second boiling prompted by massive crystallization of tourmaline from the tourmaline layer in
641 the boundary between the core margin and the core zone. The sudden depletion in B
642 experienced by the melt could decrease its capability to keep H₂O dissolved (London, 1990)
643 with part of it exsolving in discrete H₂O-rich batches related to these pockets that present an
644 intermediate paragenesis with no Li-bearing minerals.

645 As indicated above, the Li-rich pockets including purple apatite crystals are interpreted to
646 correspond to the latest pocket generation. These pockets are hosted by the most
647 fractionated pods of the core zone, which are constituted by Li-F±B±P-rich phases. The
648 dramatic depletion of B, Li, F, and P fluxes in the residual melt could again induce the
649 exsolution of H₂O-rich fluids, which would be quite enriched in Li and other incompatible
650 elements, and strongly depleted in Mn and REE at that stage of crystallization. In these
651 pockets, the only sink for Sr would be apatite, which shows some of the highest
652 concentrations (Figs. 7e, 8b, c).

653 Finally, since apatite is the only mineral phase identified in the seams, this makes it
654 more difficult to determine their timing. In this case, apatite presents intermediate Fe, Mn,
655 and REE values between those of the apatite from the Li-poor and Li-rich pockets. Taking
656 into account that REE decrease with fractionation, these seams could have formed at some
657 point between the formation of the Li-poor and Li-rich pockets. However, the presence of

658 apatite as their only phase would involve the exsolution of a fluid phase just containing P and
659 Ca as main elements, which seems difficult to explain for such relatively high degrees of
660 fractionation. Another possibility could be that the formation of these seams was related to
661 the activity of late hydrothermal fluids that autometasomatized some portions of the
662 pegmatite, mainly the core margin and the core zone, causing albitization and greisenization.
663 During albitization, Ca and P (+Sr, Y and REE) would have been leached from plagioclase.
664 Those fluids could have then precipitated apatite in fractures and vugs, giving rise to the
665 apatite-rich seams, which always occur hosted by vuggy albite from the core margin or
666 blocky feldspar from the core zone. Nevertheless, the origin of the seams is not completely
667 understood at present.

668 The chemistry of apatite may also be a good indicator of the fractionation attained by the
669 pegmatites. This has been previously described for apatite associated with pegmatites and
670 leucogranites from the Central Iberian Zone (Spain and Portugal) showing different evolution
671 degrees (Roda-Robles et al. 2022). In the U-Th-P and Y-REE-Sr ternary plots (Fig. 13)
672 apatite from the most fractionated units plots significantly closer to the Pb and Sr vertex.

673

674

IMPLICATIONS

675 This study shows how a detailed petrographic and chemical characterization of apatite
676 associated with the different units of a highly fractionated, internally zoned pegmatite, may
677 help understand the crystallization history of pegmatitic melts. It is evidenced that during the
678 internal evolution of pegmatites, the apatite chemistry records variations in the fO_2 , elemental
679 fractionation, interaction with competing mineral phases, fluids activity, and exsolution
680 events. The main chemical elements in apatite that provide petrogenetic information in
681 pegmatitic rocks include Mn, Sr, the REE, and Y.

682 In this work it is also shown how the chemistry of apatite may be useful in determining
683 the degree of fractionation attained by a pegmatite. Therefore, the usefulness of this
684 phosphate as an exploration tool for pegmatites is obvious. In this sense, the two ternary
685 diagrams Y- Σ REE-Sr and U-Th-Pb may help to discriminate between apatite crystals

686 associated with pegmatitic facies showing different fractionation degrees, with apatite from
687 the most evolved facies plotting closer to the Sr and Pb vertex.

688

689

ACKNOWLEDGMENTS

690 Authors are greatly indebted to Jeff Morrison, the owner of the Havey Quarry, who has
691 always facilitated the access to the pegmatite. Moreover, he and Ray Sprague, miner and
692 previous organizer of the Maine Pegmatite Workshop, helped us during the collecting of the
693 samples, and kept us informed about all details in the pegmatite as they were mining it, even
694 providing clarifying pictures when necessary. This manuscript highly benefitted from
695 constructive review of David London, an anonymous reviewer and the Editor Daniel Harlov.
696 This research has been financially supported by the Grant RTI2018–094097-B-100 funded
697 by MCIN/AEI/ 10.13039/501100011033 and by “ERDF A way of making Europe”, by the
698 “European Union”; and by the University of the Basque Country UPV/EHU (grant
699 GIU18/084).

700

701

REFERENCES CITED

- 702 Abdullin, F., Solé, J., Solari, L., Shchepetilnikova, V., Meneses-Rocha, J.J., Pavlinova, N., and Rodríguez-
703 Trejo, A. (2016) Single-grain apatite geochemistry of Permian–Triassic granitoids and Mesozoic
704 and Eocene sandstones from Chiapas, southeast Mexico: implications for sediment provenance.
705 *International Geology Review*, 58, 1132-1157, <https://doi.org/10.1080/00206814.2016.1150212>
- 706 Abramov, S.S. (2001) Modeling of REE fractionation in the acid melt-fluoride-chloride fluid system.
707 *Doklady Earth Sciences*, 377, 198-200,
- 708 Azadbakht, Z., Lentz, D., and McFarlane, C. (2018) Apatite Chemical Compositions from Acadian-Related
709 Granitoids of New Brunswick, Canada: Implications for Petrogenesis and Metallogenesis.
710 *Minerals*, 8, <https://doi.org/10.3390/min8120598>
- 711 Baldwin, J.R., and von Knorring, O. (1983) Compositional range of Mn-garnet in zoned granitic
712 pegmatites. *Canadian Mineralogist*, 21, 683-688,
- 713 Bau, M. (1996) Controls on the fractionation of isovalent trace elements in magmatic and aqueous systems:
714 evidence from Y/Ho, Zr/Hf, and lanthanide tetrad effect. *Contributions to Mineralogy and*
715 *Petrology*, 123, 323-333, <https://doi.org/10.1007/s004100050159>
- 716 Belousova, E.A., Griffin, W.L., O'Reilly, S.Y., and Fisher, N.I. (2002) Apatite as an indicator mineral for
717 mineral exploration: Trace-element compositions and their relationship to host rock type. *Journal*
718 *of Geochemical Exploration*, 76, 45-69, [https://doi.org/10.1016/S0375-6742\(02\)00204-2](https://doi.org/10.1016/S0375-6742(02)00204-2)
- 719 Bradley, D., Shea, E., Buchwaldt, R., Bowring, S., Benowitz, J., O'Sullivan, P., and McCauley, A. (2016)
720 Geochronology and tectonic context of lithium-cesium-tantalum pegmatites in the Appalachians.
721 *Canadian Mineralogist*, 54, 945-969, <https://doi.org/10.3749/canmin.1600035>
- 722 Bradley, D.C., Tucker, R.D., Lux, D.R., Harris, A.G., and McGregor, D.C. (1998) Migration of the Acadian
723 orogen and foreland basin across the northern Appalachians. In O.-F.R. U.S. Geological Survey,
724 Ed, 98-770, p. 79.

- 725 Bromiley, G.D. (2021) Do concentrations of Mn, Eu and Ce in apatite reliably record oxygen fugacity in
726 magmas? *Lithos*, 384-385, <https://doi.org/10.1016/j.lithos.2020.105900>
- 727 Brown, J.A., Martins, T., and Černý, P. (2017) The Tanco Pegmatite At Bernic Lake, Manitoba. Xvii.
728 Mineralogy and Geochemistry of Alkali Feldspars. *Canadian Mineralogist*, 55, 483-500,
729 <https://doi.org/10.3749/canmin.1700008>
- 730 Brown, M., and Solar, G.S. (1998) Shear-zone systems and melts: feedback relations and self-organization
731 in orogenic belts. *Journal of Structural Geology*, 28, 211-227,
- 732 Burnham, A.D., and Berry, A.J. (2014) The effect of oxygen fugacity, melt composition, temperature and
733 pressure on the oxidation state of cerium in silicate melts. *Chemical Geology*, 366, 52-60,
734 <https://doi.org/10.1016/j.chemgeo.2013.12.015>
- 735 Cao, M., Li, G., Qin, K., Seitmuratova, E.Y., and Liu, Y. (2012) Major and trace element characteristics of
736 apatites in granitoids from central Kazakhstan: Implications for petrogenesis and mineralization.
737 *Resource Geology*, 62, 63-83, <https://doi.org/10.1111/j.1751-3928.2011.00180.x>
- 738 Cao, M.-J., Zhou, Q.-F., Qin, K.-Z., Tang, D.-M., and Evans, N.J. (2013) The tetrad effect and
739 geochemistry of apatite from the Altay Koktokay No. 3 pegmatite, Xinjiang, China: implications
740 for pegmatite petrogenesis. *Mineralogy and Petrology*, 107, 985-1005,
741 <https://doi.org/10.1007/s00710-013-0270-x>
- 742 Černý, P., Ed. (1982) Granitic pegmatites in science and industry. Short Course Handbook, 8. Mineral.
743 Assoc. Canada, Winnipeg, 555p, -
- 744 Černý, P., Meintzer, R.E., and Anderson, A.J. (1985) Extreme fractionation in rare-element granitic
745 pegmatites; selected examples of data and mechanisms. *Canadian Mineralogist*, 23, 381-421,
- 746 Chu, M.-F., Wang, K.-L., Griffin, W.L., Chung, S.-L., O'Reilly, S.Y., Pearson, N.J., and Iizuka, Y. (2009)
747 Apatite Composition: Tracing Petrogenetic Processes in Transhimalayan Granitoids. *Journal of*
748 *Petrology*, 50, 1829-1855, <https://doi.org/10.1093/petrology/egp054>
- 749 Ding, T., Ma, D., Lu, J., and Zhang, R. (2015) Apatite in granitoids related to polymetallic mineral deposits
750 in southeastern Hunan Province, Shi-Hang zone, China: Implications for petrogenesis and
751 metallogenesis. *Ore Geology Reviews*, 69, 104-117,
752 <https://doi.org/10.1016/j.oregeorev.2015.02.004>
- 753 Drake, M.J., and Weill, D.F. (1975) Partition of Sr, Ba, Ca, Y, Eu²⁺, Eu³⁺, and other REE between
754 plagioclase feldspar and magmatic liquid: an experimental study. *Geochimica et Cosmochimica*
755 *Acta*, 39, 689-712, [https://doi.org/10.1016/0016-7037\(75\)90011-3](https://doi.org/10.1016/0016-7037(75)90011-3)
- 756 Garate-Olave, I., Roda-Robles, E., Gil-Crespo, P.P., and Pesquera, A. (2018) Mica and feldspar as
757 indicators of the evolution of a highly evolved granite-pegmatite system in the Tres Arroyos area
758 (Central Iberian Zone, Spain). *Journal of Iberian Geology*, 44, 375-403,
759 <https://doi.org/10.1007/s41513-018-0077-z>
- 760 García Serrano, J., Roda-Robles, E., Villaseca, C., and Simmons, W. (2017) Fe-Mn-(Mg) distribution in
761 primary phosphates and silicates, and implications for the internal evolution of the Emmons rare-
762 element pegmatite (Maine, USA). PEG2017, Abstracts and Proceedings of the Geological Society
763 of Norway, 2, p. 37-40, Kristiansand, Norway.
- 764 Goldoff, B., Webster, J.D., and Harlov, D.E. (2012) Characterization of fluor-chlorapatites by electron
765 probe microanalysis with a focus on time-dependent intensity variation of halogens. *American*
766 *Mineralogist*, 97, 1103-1115, <https://doi.org/10.2138/am.2012.3812>
- 767 Guidotti, C.V. (1989) Metamorphism in Maine: an overview. In R.D. Tucker, and R.G. Marvinney, Eds.
768 *Studies in Maine Geology*. 3, p. 1-19. Maine Geological Survey, Augusta, Maine.
- 769 -. (1993) H₂O solubility in haplogranitic melts; compositional, pressure, and temperature dependence.
770 Geological Society of America, Northeastern Section Meeting, Abstracts with Programs, 25, A21,
- 771 Harlov, D.E. (2015) Apatite: A Fingerprint for Metasomatic Processes. *Elements*, 11, 171-176,
772 <https://doi.org/10.2113/gselements.11.3.171>
- 773 Hernández-Filiberto, L., Roda-Robles, E., Simmons, W.B., and Webber, K.L. (2021) Garnet as Indicator of
774 Pegmatite Evolution: The Case Study of Pegmatites from the Oxford Pegmatite Field (Maine,
775 USA). *Minerals*, 11, <https://doi.org/10.3390/min11080802>

- 776 Icenhower, J., and London, D. (1996) Experimental partitioning of Rb, Cs, Sr, and Ba between alkali
777 feldspar and peraluminous melt. American Mineralogist, 81, 719-734, [https://doi.org/10.2138/am-](https://doi.org/10.2138/am-1996-5-619)
778 [1996-5-619](https://doi.org/10.2138/am-1996-5-619)
- 779 Irber, W. (1999) The lanthanide tetrad effect and its correlation with K/Rb, Eu/Eu*, Sr/Eu, Y/Ho, and Zr/Hf
780 of evolving peraluminous granite suites. Geochimica et Cosmochimica Acta, 63, 489-508,
781 [https://doi.org/10.1016/S0016-7037\(99\)00027-7](https://doi.org/10.1016/S0016-7037(99)00027-7)
- 782 Jahns, R. (1982) Internal Evolution of Pegmatite Bodies. In P. Černý, Ed. Granitic Pegmatites in Science
783 and Industry, v8, p. 293-327. Mineralogical Association of Canada, Ottawa.
- 784 Jahns, R.H., and Burnham, C.W. (1969) Experimental Studies of Pegmatite Genesis .1. A Model for
785 Derivation and Crystallization of Granitic Pegmatites. Economic Geology, 64, 843-864,
786 <https://doi.org/10.2113/gsecongeo.64.8.843>
- 787 Jolliff, B.L., Papike, J.J., Shearer, C.K., and Shimizu, N. (1989) Inter- and intra-crystal REE variations in
788 apatite from the Bob Ingersoll pegmatite, Black Hills, South Dakota. Geochimica et
789 Cosmochimica Acta, 53, 429-441, [https://doi.org/10.1016/0016-7037\(89\)90394-3](https://doi.org/10.1016/0016-7037(89)90394-3)
- 790 Kawabe, I. (1995) Tetrad effects and fine structures of REE abundance patterns of granitic and rhyolitic
791 rocks: ICP-AES determinations of REE and Y in eight GSJ reference rocks. Geochemical Journal,
792 29, 213-230, <https://doi.org/10.2343/geochemj.29.213>
- 793 Kontak, D.J., and Martin, R.F. (1997) Alkali feldspar in the peraluminous South Mountain Batholith, Nova
794 Scotia: Trace-element data. Canadian Mineralogist, 35, 959-977,
- 795 London, D. (1990) Internal differentiation of rare-element pegmatites: a synthesis of recent research. In
796 Stein, H.J., Hannah, J.L. (Eds.), Ore-Bearing Granite Systems; Petrogenesis and Mineralizing
797 Processes. Geological Society of America Special Paper, 246, 35-50,
- 798 -. (2005) Granitic pegmatites: an assessment of current concepts and directions for the future. Lithos, 80,
799 281-303, <https://doi.org/10.1016/j.lithos.2004.02.009>
- 800 -. (2008) Pegmatites. 347 p. The Canadian Mineralogist, Special Publication n° 10,
801 <https://doi.org/10.2138/am.2009.546>
- 802 London, D., Evensen, J.M., Fritz, E., Icenhower, J.P., Morgan VI, G.B., and Wolf, M.B. (2001a)
803 Enrichment and accommodation of manganese in granite-pegmatite systems. Geochimica Et
804 Cosmochimica Acta, Eleventh Annual V. M. Goldschmidt Conference, May 20-24, 2001, Hot
805 Springs, Virginia. Abstract n° 3369,
- 806 London, D., Hunt, L.E., and Duval, C.L. (2020) Temperatures and duration of crystallization within gem-
807 bearing cavities of granitic pegmatites. Lithos, 360-361, 105417,
808 <https://doi.org/10.1016/j.lithos.2020.105417>
- 809 London, D., Morgan, G.B., Paul, K.A., and Guttery, B.M. (2012) Internal Evolution of Mirolitic Granitic
810 Pegmatites at the Little Three Mine, Ramona, California, USA. Canadian Mineralogist, 50, 1025-
811 1054, <https://doi.org/10.3749/canmin.50.4.1025>
- 812 London, D., Morgan Vi, G.B., and Wolf, M.B. (2001b) Amblygonite-montebbrasite solid solutions as
813 monitors of fluorine in evolved granitic and pegmatitic melts. American Mineralogist, 86, 225-233,
814 <https://doi.org/10.2138/am-2001-2-303>
- 815 Maner, J.L., London, D., and Icenhower, J.P. (2019) Enrichment of manganese to spessartine saturation in
816 granite-pegmatite systems. American Mineralogist, 104, 1625-1637, [https://doi.org/10.2138/am-](https://doi.org/10.2138/am-2019-6938)
817 [2019-6938](https://doi.org/10.2138/am-2019-6938)
- 818 McDonough, W., and Sun, S.S. (1995) The composition of the Earth. Chemical Geology, 67, 1050-1056,
819 [https://doi.org/10.1016/0009-2541\(94\)00140-4](https://doi.org/10.1016/0009-2541(94)00140-4)
- 820 Miles, A.J., Graham, C.M., Hawkesworth, C.J., Gillespie, M.R., and Hinton, R.W. (2013) Evidence for
821 distinct stages of magma history recorded by the compositions of accessory apatite and zircon.
822 Contributions to Mineralogy and Petrology, 166, 1-19, <https://doi.org/10.1007/s00410-013-0862-9>
- 823 Miles, A.J., Graham, C.M., Hawkesworth, C.J., Gillespie, M.R., Hinton, R.W., and Bromiley, G.D. (2014)
824 Apatite: A new redox proxy for silicic magmas? Geochimica et Cosmochimica Acta, 132, 101-119,
825 <https://doi.org/10.1016/j.gca.2014.01.040>

- 826 Moench, R.H., Boone, G.M., Bothner, W.A., Boudette, E.L., Hatch Jr, N.L., Hussey Iii, A.M., and
827 Marvinney, R.G. (1995) Geologic map of the Sherbrooke-Lewiston area, Maine, New Hampshire,
828 and Vermont, United States, and Quebec, Canada. *IMAP*.
- 829 Monecke, T., Kempe, U., Monecke, J., Sala, M., and Wolf, D. (2002) Tetrad effect in rare earth element
830 distribution patterns: A method of quantification with application to rock and mineral samples from
831 granite-related rare metal deposits. *Geochimica et Cosmochimica Acta*, 66, 1185-1196,
- 832 Müller, A., Keyser, W., Simmons, W.B., Webber, K., Wise, M., Beurlen, H., Garate-Olave, I., Roda-Robles,
833 E., and Galliski, M.Á. (2021) Quartz chemistry of granitic pegmatites: Implications for
834 classification, genesis and exploration. *Chemical Geology*, 584, [https://doi.org/](https://doi.org/10.1016/j.chemgeo.2021.120507)
835 [10.1016/j.chemgeo.2021.120507](https://doi.org/10.1016/j.chemgeo.2021.120507)
- 836 Munoz, J.L. (1984) F-OH and Cl-OH exchange in micas with applications to hydrothermal ore deposits. In
837 S.W. Bailey, Ed. *Micas*, p. 469-493. *Reviews in Mineralogy & Geochemistry*, vol. 13.
838 Mineralogical Society of America.
- 839 Nicholson, S.W., Dicken, C.L., Horton, J.D., Foose, M.P., Mueller, J.A.L., and Hon, R. (2006) Preliminary
840 integrated geologic map databases for the United States: Connecticut, Maine, Massachusetts, New
841 Hampshire, New Jersey, Rhode Island and Vermont. USGS Open-File Report: 2006-1272,
- 842 Osberg, P.H. (1978) Synthesis of the geology of the northeast Appalachians, U.S.A. In P.E. Schenk, and
843 E.T. Tosier, Eds. *Appalachian-Caledonide orogen*. Geological Survey of Canada, Paper 78-13, p.
844 137-167.
- 845 Osberg, P.H., Hussey, A.M.I., and Boone, G.H. (1985) Bedrock Geologic Map of Maine. Maine Geol Surv,
846 1:500,000 scale map,
- 847 Pan, L.-C., Hu, R.-Z., Wang, X.-S., Bi, X.-W., Zhu, J.-J., and Li, C. (2016) Apatite trace element and
848 halogen compositions as petrogenetic-metallogenic indicators: Examples from four granite plutons
849 in the Sanjiang region, SW China. *Lithos*, 254-255, 118-130,
850 <https://doi.org/10.1016/j.lithos.2016.03.010>
- 851 Pan, Y., and Fleet, M.E. (2002) Compositions of the Apatite-Group Minerals: Substitution Mechanisms and
852 Controlling Factors. *Reviews in Mineralogy and Geochemistry*, 48, 13-49,
853 <https://doi.org/10.2138/rmg.2002.48.2>
- 854 Paton, C., Hellstrom, J., Paul, B., Woodhead, J., and Hergt, J. (2011) Iolite: Freeware for the visualisation
855 and processing of mass spectrometric data. *Journal of Analytical Atomic Spectrometry*, 26,
856 <https://doi.org/10.1039/c1ja10172b>
- 857 Paul, B., Paton, C., Norris, A., Woodhead, J., Hellstrom, J., Hergt, J., and Greig, A. (2012) CellSpace: A
858 module for creating spatially registered laser ablation images within the Iolite freeware
859 environment. *Journal of Analytical Atomic Spectrometry*, 27, <https://doi.org/10.1039/c2ja10383d>
- 860 Peretyazhko, I.S., and Savina, E.A. (2010) Tetrad effects in the rare earth element patterns of granitoid
861 rocks as an indicator of fluoride-silicate liquid immiscibility in magmatic systems. *Petrology*, 18,
862 514-543, <https://doi.org/10.1134/s086959111005005x>
- 863 Pouchou, J.L., and Pichoir, F. (1985) "PAP" $\phi(\rho Z)$ procedure for improved quantitative microanalysis. In
864 J.T. Armstrong, Ed. *Microbeam Analysis*, p. 104-106. San Francisco Press.
- 865 Reusch, D.N., and van Staal, C.R. (2011) The Dog Bay – Liberty Line and its significance for Silurian
866 tectonics of the northern Appalachian orogen. *Canadian Journal of Earth Sciences*, 49, 239-258,
867 <https://doi.org/10.1139/e11-024>
- 868 Roda-Robles, E., Gil-Crespo, P.P., Pesquera, A., Lima, A., Garate-Olave, I., Merino-Martínez, E., Cardoso-
869 Fernandes, J., and Errandonea-Martin, J. (2022) Compositional Variations in Apatite and
870 Petrogenetic Significance: Examples from Peraluminous Granites and Related Pegmatites and
871 Hydrothermal Veins from the Central Iberian Zone (Spain and Portugal). *Minerals*, 12, 1401,
872 <https://doi.org/10.3390/min12111401>
- 873 Roda-Robles, E., Pesquera, A., Gil-Crespo, P., and Torres-Ruiz, J. (2012) From granite to highly evolved
874 pegmatite: A case study of the Pinilla de Fermoselle granite–pegmatite system (Zamora, Spain).
875 *Lithos*, 153, 192-207, <https://doi.org/10.1016/j.lithos.2012.04.027>
- 876 Roda-Robles, E., Pesquera, A., Gil-Crespo, P.P., Simmons, W., and Falster, A. (2017) Textural and chemical
877 variations of garnet and apatite recording the internal evolution of the Berry-Havey rare-element

- 878 pegmatite (Maine, USA): preliminary results. Abstracts and Proceedings of the 8th International
879 Symposium on Granitic Pegmatites (Kristiansand, Norway), 107-110,
- 880 Roda-Robles, E., Pesquera, A., Gil-Crespo, P.P., Torres-Ruiz, J., and De Parseval, P. (2006) Mineralogy and
881 geochemistry of micas from the Pinilla de Fermoselle pegmatite (Zamora, Spain). European
882 Journal of Mineralogy, 18, 369-377,
- 883 Roda-Robles, E., Simmons, W., Pesquera, A., Gil-Crespo, P.P., Nizamoff, J., and Torres-Ruiz, J. (2015a)
884 Micas associated with the Berry-Havey pegmatite (Maine, USA): chemical and textural variation,
885 and significance for the pegmatite internal evolution. 7th International Symposium on Granitic
886 Pegmatites-PEG2015, p. 79-80, Ksiaz, Poand.
- 887 Roda-Robles, E., Simmons, W., Pesquera, A., Gil-Crespo, P.P., Nizamoff, J., and Torres-Ruiz, J. (2015b)
888 Tourmaline as a petrogenetic monitor of the origin and evolution of the Berry-Havey pegmatite
889 (Maine, U.S.A.). American Mineralogist, 100, 95-109, <https://doi.org/10.2138/am-2015-4829>
- 890 Sha, L.K., and Chappell, B.W. (1999) Apatite chemical composition, determined by electron microprobe
891 and laser-ablation inductively coupled plasma mass spectrometry, as a probe into granite
892 petrogenesis. Geochimica Et Cosmochimica Acta, 63, 3861-3881, [https://doi.org/10.1016/s0016-7037\(99\)00210-0](https://doi.org/10.1016/s0016-7037(99)00210-0)
- 894 Simmons, W., Falster, A., Webber, K., Felch, M., and Bradley, D. (2017) Lithium-Boron-Beryllium Gem
895 Pegmatites, Oxford Co., Maine: Havey and Mount Mica Pegmatites. New England Intercollegiate
896 Geological Conference 2017, p. 1-34.
- 897 Simmons, W., Falster, A., Webber, K., Roda-Robles, E., Boudreaux, A.P., Grassi, L.R., and Freeman, G.
898 (2016) Bulk Composition of Mt. Mica Pegmatite, Maine, USA: Implications For the Origin of An
899 LCT Type Pegmatite By Anatexis. Canadian Mineralogist, 54, 1053-1070,
900 <https://doi.org/10.3749/canmin.1600017>
- 901 Smith, J.V. (1974) Feldspar Minerals, v2 Chemical and Textural Properties. 692 p. Springer Berlin,
902 Heidelberg, <https://doi.org/10.1007/978-3-642-65743-6>
- 903 Sokolov, Y.M., and Khlestov, V.V. (1990) Garnets as indicators of the physicochemical conditions of
904 pegmatite formation. International Geology Review, 32, 1095-1107, <https://doi.org/10.1080/00206819009465842>
- 906 Solar, G.S., and Brown, M. (2001) Deformation partitioning during transpression in response to Early
907 Devonian oblique convergence, northern Appalachian orogen, USA. Journal of Structural Geology,
908 23, 1043-1065, [https://doi.org/10.1016/S0191-8141\(00\)00175-9](https://doi.org/10.1016/S0191-8141(00)00175-9)
- 909 Solar, G.S., and Tomascak, P.B. (2001) Is there a relation between transpressive deformation and pluton
910 emplacement in southern Maine? Geological Society of America, Abstracts with Programs, 33.
- 911 -. (2009) The Sebago Pluton and the Sebago Migmatite Domain, southern Maine; results from new studies.
912 2009 Annual Meeting of Northeastern Section, Geol Soc Amer, Field Trip 2, 1-24,
- 913 -. (2016) The Migmatite-Granite Complex of Southern Maine: Its Structure, Petrology, Geochemistry,
914 Geochronology, and Relation to the Sebago Pluton. In H.N. Berry, IV, and D.P. West, Jr., Eds.
915 Guidebook for field trips along the Maine coast from Maquoit Bay to Muscongus Bay: New
916 England Intercollegiate Geological Conference, p. 19-42.
- 917 Tomascak, P.B., Krogstad, E.J., and Walker, R.J. (1996a) Nature of the crust in Maine, USA: evidence from
918 the Sebago batholith. Contributions to Mineralogy and Petrology, 125, 45-59,
919 <https://doi.org/10.1007/s004100050205>
- 920 Tomascak, P.B., Krogstad, E.J., and Walker, R.J. (1996b) U-Pb Monazite Geochronology of Granitic Rocks
921 from Maine: Implications for Late Paleozoic Tectonics in the Northern Appalachians. The Journal
922 of Geology, 104, 185-195,
- 923 Veksler, I.V., and Thomas, R. (2002) An experimental study of B-, P- and F-rich synthetic granite pegmatite
924 at 0.1 and 0.2 GPa. Contributions to Mineralogy and Petrology, 143, 673-683,
- 925 Warr, L.N. (2021) IMA–CNMNC approved mineral symbols. Mineralogical Magazine, 85, 291-320,
926 <https://doi.org/10.1180/mgm.2021.43>
- 927 Webber, K.L., Simmons, W.B., Falster, A.U., and Hanson, S.L. (2019) Anatectic pegmatites of the Oxford
928 County pegmatite field, Maine, USA. Canadian Mineralogist, 57, 811-815,
929 <https://doi.org/10.3749/canmin.AB00028>

- 930 Webster, J.D., and Piccoli, P.M. (2015) Magmatic Apatite: A Powerful, Yet Deceptive, Mineral. *Elements*,
931 11, 177-182, <https://doi.org/10.2113/gselements.11.3.177>
- 932 Wise, M.A., and Brown, C.D. (2010) Mineral chemistry, petrology and geochemistry of the Sebago granite-
933 pegmatite system, Southern Maine, USA. *Journal of Geosciences*, 55, 3-26, [https://doi.org/](https://doi.org/10.3190/jgeosci.061)
934 10.3190/jgeosci.061
- 935 Wones, D.R., and Eugster, H.P. (1965) Stability of biotite: Experiment, Theory, and Application. *The*
936 *American mineralogist*, 50, 1228-1272,
- 937 Yu, M., Xia, Q.-X., Zheng, Y.-F., Zhao, Z.-F., Chen, Y.-X., Chen, R.-X., Luo, X., Li, W.-C., and Xu, H.
938 (2021) The composition of garnet in granite and pegmatite from the Gangdese orogen in
939 southeastern Tibet: Constraints on pegmatite petrogenesis. *American Mineralogist*, 106, 265-281,
940 <https://doi.org/10.2138/am-2020-7388>
- 941 Zhao, Z., Xiong, X., Han, X., Wang, Y., Wang, Q., Bao, Z., and Borming, J. (2002) Controls on the REE
942 tetrad effect in granites: Evidence from the Qianlishan and Baerzhe Granites, China. *Geochemical*
943 *Journal*, 36, 527-543, <https://doi.org/10.2343/geochemj.36.527>

944

945

946 **FIGURE CAPTIONS:**

947 **Fig. 1.** (a) Map showing the location of the Migmatite-Granite-Complex in New England
948 and (b) the principal geological features of the area and location of the Berry-Havey
949 pegmatite.

950

951 **Fig. 2.** Schematic map with two cross sections of the Berry-Havey pegmatite.

952

953 **Fig. 3.** (a) Microphotograph of a subhedral apatite crystal from the Wall Zone (under
954 plane-polarized light). (b) Dark bluish apatite crystals intergrowth with garnet from the garnet
955 layer, in the limit between the Intermediate Zone and the Core Margin. (c) Microphotograph
956 of some subhedral apatite crystals from a pod of the Core Zone (under crossed-polarized
957 light). (d) Seam filled by purple apatite hosted by blocky feldspar in the Core Zone. (e)
958 Strongly zoned grayish-white apatite euhedral lenses over quartz from a Li-poor pocket. (f)
959 Euhedral purple prism of apatite over a mass of albite and pinkish lepidolite from a Li-rich
960 pocket.

961

962 **Fig. 4.** Major element variations in apatite from the different units distinguished in the
963 Berry-Havey pegmatite: (a) F; (b) Mn^{2+} ; and (c) Ca. (All values in a.p.f.u.).

964

965 **Fig. 5.** Binary plots for apatite from the different units of the Berry-Havey pegmatite (all
966 the values are in a.p.f.u.): (a) Ca versus Mn^{2+} ; (b) Fe^{2+} versus Mn^{2+} ; and (c) Ca versus Fe^{2+} .
967

968 **Fig. 6.** Representative chemical zoning patterns for the major elements in zoned apatite
969 crystals (left: grayish-white crystal from a Li-poor pocket; and right: purple-green crystal from
970 a seam). (a) Mn^{2+} , (b) Fe^{2+} , and (c) Ca. (All values are in a.p.f.u.).

971
972 **Fig. 7.** Variations in the main trace elements in apatite from the different units
973 distinguished in the Berry-Havey pegmatite. (All values in ppm) (Legend as in Fig. 4).

974
975 **Fig. 8.** Binary plots of main trace elements in apatite (all values in ppm): (a) ΣREE
976 versus Y; (b) Sr versus ΣREE ; (c) Sr versus Y; (d) Pb versus Th; (e) Th versus U; (f) Pb
977 versus U; (g) Ho versus Y; and (h) Hf versus Zr.

978
979 **Fig. 9.** Representative chemical zoning patterns for main trace elements in zoned
980 apatite crystals (left: grayish-white crystal from a Li-poor pocket; and right: purple-green
981 crystal from a seam). (All values in ppm).

982
983 **Fig. 10.** Chondrite-normalized (McDonough and Sun, 1995) lanthanide patterns for: (a)
984 apatite from the wall zone, the intermediate zone, the core margin, and the purple apatite
985 from the Li-rich pockets in the core zone; (b) zoned grayish-white apatite lenses from Li-poor
986 pockets in the core zone; and, (c) and (d) zoned purple-green apatite crystals from the
987 seams. (Legend as in Fig. 4).

988
989 **Fig. 11.** Binary plots of (a) the Eu anomaly, (defined as $Eu/Eu^* = Eu_n / (Sm_n \times Gd_n)^{0.5}$)
990 and the $TE_{1,3}$ value for the tetrad effects calculated according to the procedure of Irber
991 (1999); and (b) Y (ppm) versus $TE_{1,3}$. (Legend as in Fig. 4).

992

993 **Fig. 12.** Binary plots of (a) the Ce anomaly (defined as $Ce/Ce^* = Eu_n/(La_n \times Pr_n)^{0.5}$)
994 versus the Eu anomaly (defined as $Eu/Eu^* = Eu_n/(Sm_n \times Gd_n)^{0.5}$), and (b) Y/Ho versus Y (in
995 ppm). The grayish area represents the region where the Y/Ho ratios correspond to CHARAC
996 values. (Legend as in Fig. 4).

997

998 **Fig. 13.** Triangular plots for apatite: (a) Pb-U-Th; and, (b) Sr-Y- Σ REE, for the different
999 units distinguished in the Berry-Havey pegmatite. (Legend as in Fig. 4).

1000

1001 **TABLE CAPTIONS:**

1002 **Table 1.** Main characteristics of the Berry-Havey pegmatite zones and the associated
1003 apatite.

1004 **Table 2.** Representative microprobe analyses with major element composition (wt%)
1005 and unit formula (a.p.f.u.) calculated on the basis of 26 (O,F,Cl,OH), H₂O* estimated, for
1006 apatite associated with the different units distinguished in the Berry-Havey pegmatite.

1007 **Table 3.** Representative trace element analyses (values in ppm) for apatite associated
1008 with the different units distinguished in the Berry-Havey pegmatite.

ZONE		MINERALS*	GENERAL TEXTURES	APATITE TEXTURE	APATITE CHEMISTRY (ppm)
WALL ZONE		Qz, Kfs, Pl, Bt, Ms ± Grt ± Srl ± Ap	Homogeneous, very fine to medium grained facies. Locally gneissic facies	Fine grained whitish subhedral crystals < 5 mm	Fluorapatite ΣREE: 1796-2178 Y: 1155-1503 Sr: 49.9-52.5
INTERMEDIATE ZONE		Qz, Kfs, Pl ± Grt ± Bt ± Srl ± Ap	Qz-Kfs graphic intergrowths (> 85% volume)	Fine grained whitish anhedral crystals < 5 mm	Fluorapatite ΣREE: 1219-1286 Y: 225-261 Sr: 2.9-16.1
CORE MARGIN		Ab, Qz, Srl ± green-Elb ± Grt ± Ap	Matrix of tabular crystals of cleveandite ("vuggy" Ab), where coarse tourmaline tapered prismatic crystals occur. Grt layer	Medium sized bluish-greenish prismatic or anhedral crystals < 5 cm Intergrowth with Grt in the Grt layer	Mn-rich fluorapatite ΣREE: 309-355 Y: 22.7-26.3 Sr: 87-23.4
CORE ZONE pods		Qz, Kfs, Ab, Lpd, Ms, Li-Ms, Mbs, Brl, Fe-Mn Phosphates, Ross-Elb, ± Cst ± Clb-Ttl ± Ap	Blocky Qz, Kfs, and Ab. Purple fine-grained or book Lpd. Coarse book Ms rimmed by Lpd. Multicoloured tourmaline prisms. Fe-Mn-phosphates or Mbs sub-rounded pods	Fine-sized prismatic crystals with a concentric optical zoning	Fluorapatite ΣREE: 0-0.14 Y: 0 Sr: 27-1614
CORE ZONE Pockets	Li-poor pockets	Qz, Kfs, Ab, Srl, Ap	Blocky Qz and Kfs, "vuggy" Ab. Sub to euhedral smoky Qz, Etched dark tourmaline	Hexagonal zoned lenses with a greyish-light blue core and a white rim (≈1 cm Ø)	Mn-rich fluorapatite ΣREE: 9.55-983 Y: 31.7-979 Sr: 759-28710
	Li-rich pockets	Qz, Kfs, Ab, Lpd, Li-Ms, Mbs, Brl, Fe-Mn Phosphates, Rsm-Elb ± Ap	Blocky Qz and Kfs, "vuggy" Ab. Multicoloured tourmaline, Lpd "pencils"	Deep purple or bluish short hexagonal prisms (≈1 cm Ø)	Fluorapatite ΣREE: 0.09-0.37 Y: 0.14-0.54 Sr: 5910-19800
	Seams	Ap	Elongated cavities (≤ 50 cm long and ≤ 20 cm wide) completely or partially filled with Ap	Anhedral purple masses or hexagonal prisms. Zoned prisms with purple core and greenish rims	Mn-rich fluorapatite ΣREE: 0.629-210 Y: 0-23 Sr: 17-3640

*Mineral symbols according to Warr (2021): Ap=apatite, Qz=quartz, Kfs= K-feldspar, Pl=plagioclase, Ms= muscovite, Grt= garnet, Srl=Schorl, Bt=biotite, Elb= elbaite, Lpd= lepidolite, Mbs= Montebasite, Brl= beryl, Rsm= rossmanite, Cst= cassiterite, Clb-Ttl= columbite-tantalite. Grain size: very fine = <6 mm; fine = 6 mm to 2.5 cm; medium = 2.5 cm to 10 cm.

Table 1

N° anal.	1	2	3	4	5	6	7	8	9	10	11	12	13
Zone	Wall Zone		Intermediate Zone		Core Margin		Core Zone (pods)		Core Zone (Li-poor Pocket)		Core Zone (Li-rich Pocket)	Core Zone (seam)	
weight(%)									grayish core	withish rim	purple	purple core	greenish rim
P ₂ O ₅	43.29	42.08	41.15	41.57	42.34	42.13	41.95	41.61	42.25	40.43	41.42	40.96	41.76
SiO ₂	0.03	0.05	-	-	0.04	0.03	0.01	0.02	-	-	-	b.d.l.	-
Al ₂ O ₃	0.02	b.d.l.	0.01	0.01	b.d.l.	b.d.l.	b.d.l.	0.01	b.d.l.	b.d.l.	b.d.l.	b.d.l.	b.d.l.
La ₂ O ₃	0.07	0.05	-	-	0.03	0.03	-	-	-	-	-	-	-
Ce ₂ O ₃	0.01	0.22	-	-	0.05	0.06	-	-	-	-	-	-	-
MgO	b.d.l.	b.d.l.	0.03	0.04	b.d.l.	b.d.l.	b.d.l.	b.d.l.	0.02	0.03	0.03	b.d.l.	b.d.l.
CaO	55.00	55.86	48.84	48.86	42.34	42.13	55.72	55.11	50.62	53.69	54.36	53.46	56.25
MnO	0.07	0.38	6.38	6.43	9.70	9.55	0.21	0.28	4.65	0.21	0.10	3.91	0.93
FeO	0.03	0.01	0.32	0.31	0.21	0.15	b.d.l.	0.03	0.31	b.d.l.	b.d.l.	0.17	0.10
SrO	0.07	b.d.l.	-	-	b.d.l.	b.d.l.	-	-	0.09	3.41	2.35	-	-
Na ₂ O	0.02	0.13	b.d.l.	b.d.l.	0.02	0.04	0.04	b.d.l.	b.d.l.	b.d.l.	b.d.l.	0.01	0.00
F	3.10	3.24	4.28	4.34	2.62	2.66	3.51	3.34	5.91	5.34	5.00	3.17	3.17
Cl	b.d.l.	0.01	0.01	b.d.l.	b.d.l.	b.d.l.	0.01	b.d.l.	0.08	b.d.l.	b.d.l.	0.08	0.03
H ₂ O*	0.34	0.26	b.d.l.	b.d.l.	0.48	0.45	0.12	0.19	b.d.l.	b.d.l.	b.d.l.	0.25	0.29
O=F	1.31	1.37	1.80	1.83	1.10	1.12	1.48	1.41	2.50	2.25	2.11	1.35	1.34
TOTAL	100.74	100.92	99.20	99.74	96.73	96.11	100.08	99.18	101.43	100.86	101.17	100.66	101.18
Structural formulae on the basis of 26 (O,F,Cl,OH)													
(a.p.f.u.)													
P	6.074	5.953	5.962	5.981	6.244	6.250	5.971	5.974	5.910	5.789	5.870	5.880	5.911
Si	0.005	0.008	-	-	0.007	0.005	0.002	0.003	-	-	-	b.d.l.	-
Al	0.005	b.d.l.	0.001	0.001	b.d.l.	b.d.l.	b.d.l.	0.002	b.d.l.	b.d.l.	b.d.l.	b.d.l.	b.d.l.
La	0.004	0.003	-	-	0.002	0.002	-	-	-	-	-	-	-
Ce ³⁺	0.001	0.013	-	-	0.003	0.004	-	-	-	-	-	-	-
Mg	b.d.l.	b.d.l.	0.008	0.011	b.d.l.	b.d.l.	b.d.l.	b.d.l.	0.006	0.008	0.008	b.d.l.	b.d.l.
Ca	9.768	10.000	8.955	8.897	7.902	7.910	10.035	10.013	8.962	9.728	9.749	9.712	10.076
Mn ²⁺	0.010	0.054	0.924	0.926	1.430	1.417	0.029	0.041	0.650	0.030	0.014	0.561	0.132
Fe ²⁺	0.004	0.001	0.046	0.044	0.030	0.021	b.d.l.	0.005	0.043	b.d.l.	b.d.l.	0.025	0.014
Sr	0.006	b.d.l.	-	-	b.d.l.	b.d.l.	-	-	0.009	0.334	0.228	-	-
Na	0.005	0.042	b.d.l.	b.d.l.	0.007	0.014	0.012	b.d.l.	b.d.l.	b.d.l.	b.d.l.	0.003	0.000
F	1.625	1.712	2.315	2.334	1.445	1.474	1.864	1.789	3.087	2.854	2.648	1.700	1.673
Cl	b.d.l.	0.003	0.003	b.d.l.	b.d.l.	b.d.l.	0.002	b.d.l.	0.021	b.d.l.	0.000	0.022	0.008
OH*	0.375	0.285	0.000	0.000	0.555	0.525	0.134	0.211	0.000	0.000	0.000	0.278	0.319
(F+Cl+OH)	2.000	2.000	2.317	2.335	2.000	2.000	2.000	2.000	3.108	2.854	2.649	2.000	2.000

n° anal.	1	2	3	4	5	6	7	8	9	10	11	12	13	14	15
Zone	Wall Zone		Intermediate Zone		Core Margin		Core Zone (pods)			Core Zone (Li-poor Pocket)		Core Zone (Li-rich Pocket)		Core Zone (Seam)	
(All values ppm)										grayish-core	whitish-rim		purple	purple core	greenish rim
Li	11.19	15.88	11.2	15.6	21.3	28.1	0	0	0	8.9	-	-	1.8	1.74	54
Be	-	0.003	0.33	6.2	6.1	2.39	-	0.85	1.71	-	-	-	0.86	-	6.6
Si	-	280	-	-	1010	1370	1480	1030	0	-	-	-	-	2250	3550
K	-	1.94	10	25	7.9	179	0	0	0	-	-	-	1.4	-	26
Sc	0.65	1.12	1.09	1.27	1.35	1.336	0.77	1.49	0	-	1.23	-	-	-	-
Ti	62.9	77	80.3	101	46.2	53.9	179.3	180.2	186.8	180	191	104	91	177.4	178
V	-	-	-	-	-	0.099	0	0	0	-	-	-	-	-	-
W	0.077	0.086	-	0.04	0.161	0.24	1.52	0.0126	1.25	0.0245	0.0027	-	0.0076	0.022	0.01
Ga	-	-	0.18	0.25	-	1.29	0.342	0.268	0.351	-	0.156	-	-	0.477	0.66
Ni	0.265	-	-	-	0.206	-	0.76	0.64	0.87	-	-	-	-	0.61	0.83
Mo	-	-	0.43	0.485	0.531	0.557	0	0.191	0	0.34	-	-	-	0.078	0.092
Zn	1.13	0.82	2.71	2.35	15.7	7.54	0	0	0.94	5.2	-	2.34	-	-	1.15
Rb	0.144	0.107	-	0.14	0.22	19.5	0	0	0	-	-	-	-	-	1.08
Sr	50.8	52.5	2.94	16.1	23.4	8.7	34.3	1614	662	759	28710	19800	9470	32.5	2094
Y	1155	1503	225	230	23.69	25.27	0	0.104	0	979	31.7	0.536	0.46	8	0.023
Zr	-	0.05	0.16	4.4	0.105	0.155	62	7.35	32.2	0.076	0.065	0.139	0.374	-	37
Nb	-	-	-	1.15	0.9	1.37	0.231	0	0.51	-	-	-	-	-	0.027
Sn	0.21	0.14	7.54	8.1	2.15	4.53	0.063	0	0	2.47	0.204	0.09	0.092	0.062	0.222
Cs	0.0331	0.0308	-	0.102	0.271	2.94	0.014	0	0	-	-	-	-	-	0.39
Ba	0.33	0.068	0.2	3.4	0.53	0.23	0.11	0	0	0.056	0.59	1.88	0.111	-	0.283
La	134	173	277	289	153.4	168	-	0.0087	-	94.3	0.28	0	0.062	12.8	0.105
Ce	413	486	628	655	138.7	162.2	-	-	0.055	268	0.462	0.011	0.0617	24.1	0.192
Pr	65.1	73.3	47.6	50.1	6.23	6.94	-	-	0.0116	28.4	0.044	0	0.0088	2.2	0.0186
Nd	279	313	77.2	79.6	5.88	6.48	-	0.0011	0.027	72.2	0.106	0	0.033	5.57	0.044
Sm	96.3	113.4	56.8	58.9	2.91	3.1	-	-	0.022	47.4	0.123	0.0073	0.0204	2.67	0.016
Eu	3.263	3.414	0.301	0.307	0.115	0.138	-	-	-	1.815	0.0283	-	0	0.553	-
Gd	128.5	160	52.7	53.8	2.48	2.7	-	-	0.021	71.9	0.252	0.006	0.024	1.63	0.0047
Tb	34.2	42.1	15.63	16.21	0.782	0.842	-	-	-	24.3	0.1452	0.0041	0.0065	0.338	0.002
Dy	273	340	58.3	59.3	3.52	3.79	-	0.0024	-	177.9	1.649	0.0167	0.046	1.76	0.004
Ho	51.9	65	2.67	2.7	0.181	0.1948	-	-	-	23.5	0.298	0.0037	0.0083	0.191	-
Er	143	183	2.28	2.29	0.243	0.271	-	0.0038	-	46.7	0.99	0.0169	0.0288	0.459	-
Tm	21.53	27.81	0.191	0.175	0.0314	0.0341	-	-	-	8.3	0.351	0.0038	0.0055	0.095	-
Yb	137	177	0.685	0.748	0.186	0.248	-	0.0023	-	50.9	4.24	0.033	0.055	0.728	-
Lu	16.6	21.63	0.0631	0.0597	0.02	0.0261	-	-	-	5.26	0.582	0.0077	0.0097	0.114	-
Hf	0.086	0.111	0.0222	0.29	0.0034	0.0115	2.72	0.725	1.31	0.058	0.0076	0.0107	0.0099	-	6.62
Ta	0.0204	0.0274	0.0013	0.0102	0.0422	0.137	0.0125	0.0016	0.0111	0.0085	-	-	-	0.0021	0.066
Tl	-	-	-	-	0.0148	0.126	-	-	-	-	-	-	-	-	0.0034
Pb	4.66	5.57	38.3	36.6	25.55	23.42	4.65	12.17	0.941	193	4.93	341	9.33	6.4	17.5
Th	0.3	0.073	52.6	56.8	166.7	190	0.0079	-	-	13.5	0.0208	-	-	0.94	0.07
U	6.07	11.15	152.5	162.5	590	153.6	0.129	0.16	49.2	26.4	108.4	3.31	0.51	0.93	3.31
ΣLREE	987	1159	1086	1133	307.00	346.72	0.00	0.01	0.12	510.00	1.02	0.02	0.19	47.34	0.38
ΣHREE	809	1020	132.8	135.6	7.56	8.24	0.00	0.01	0.02	411.00	8.54	0.09	0.18	5.87	0.01

-Below detection limit

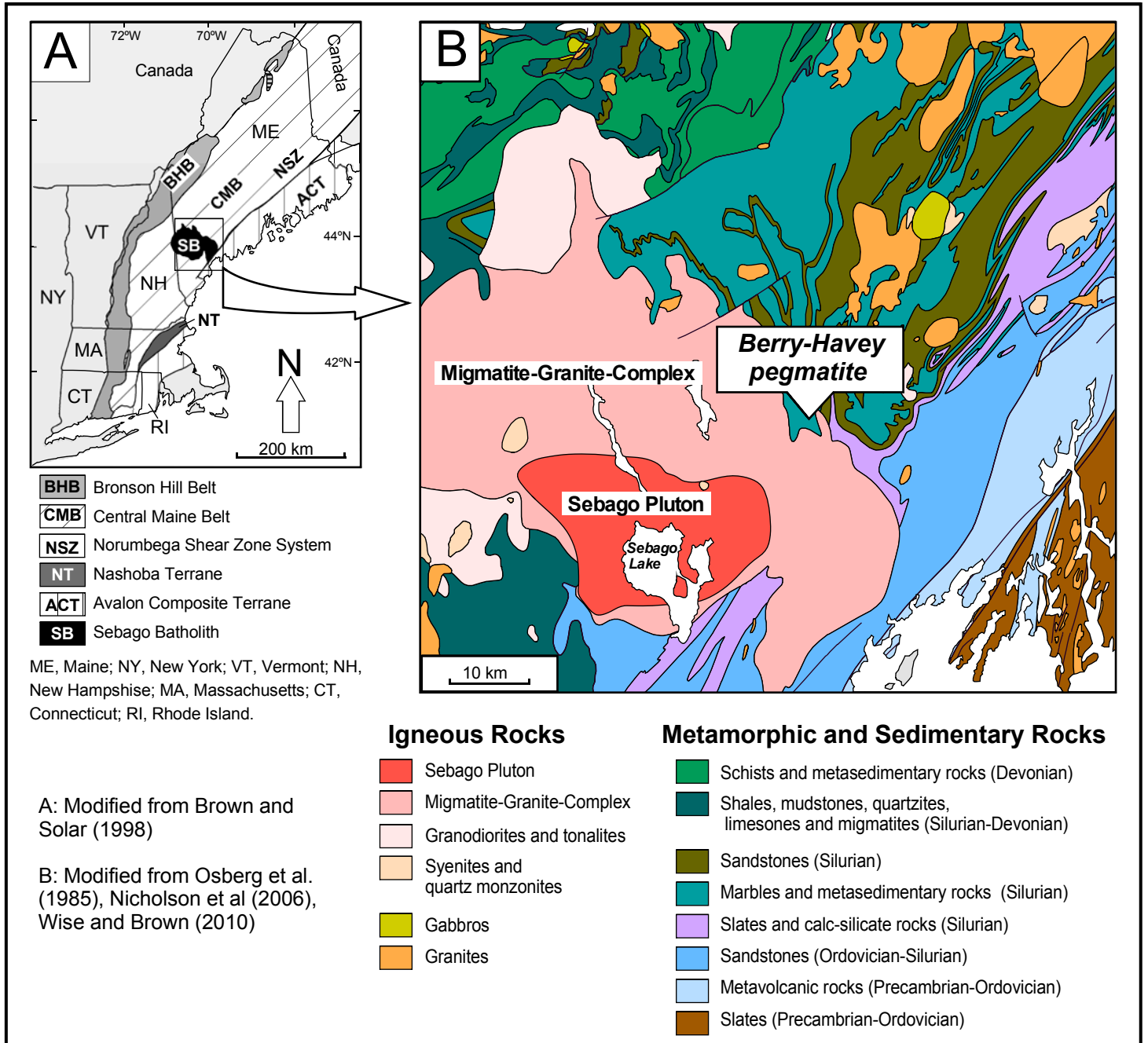


Fig. 1

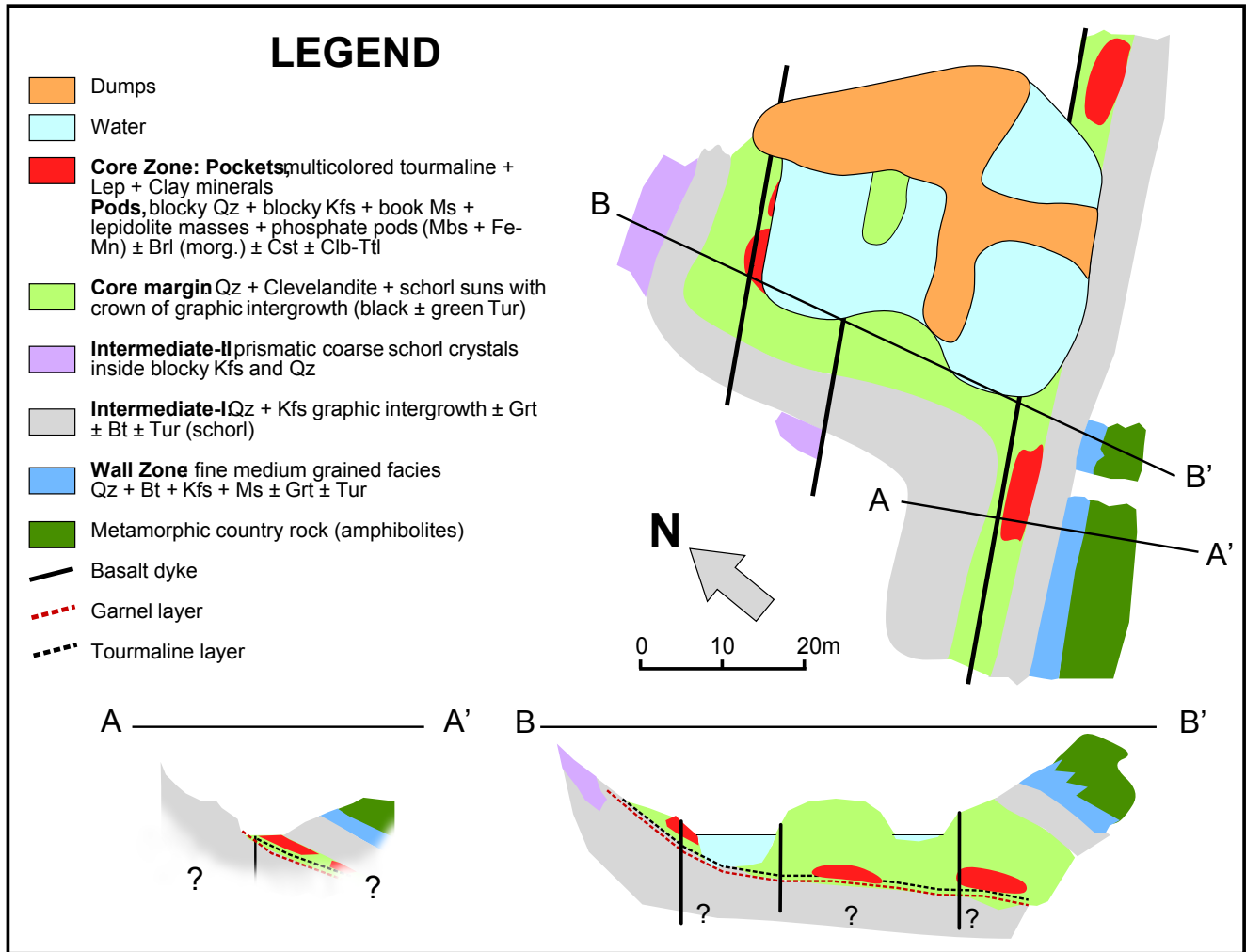


Fig. 2

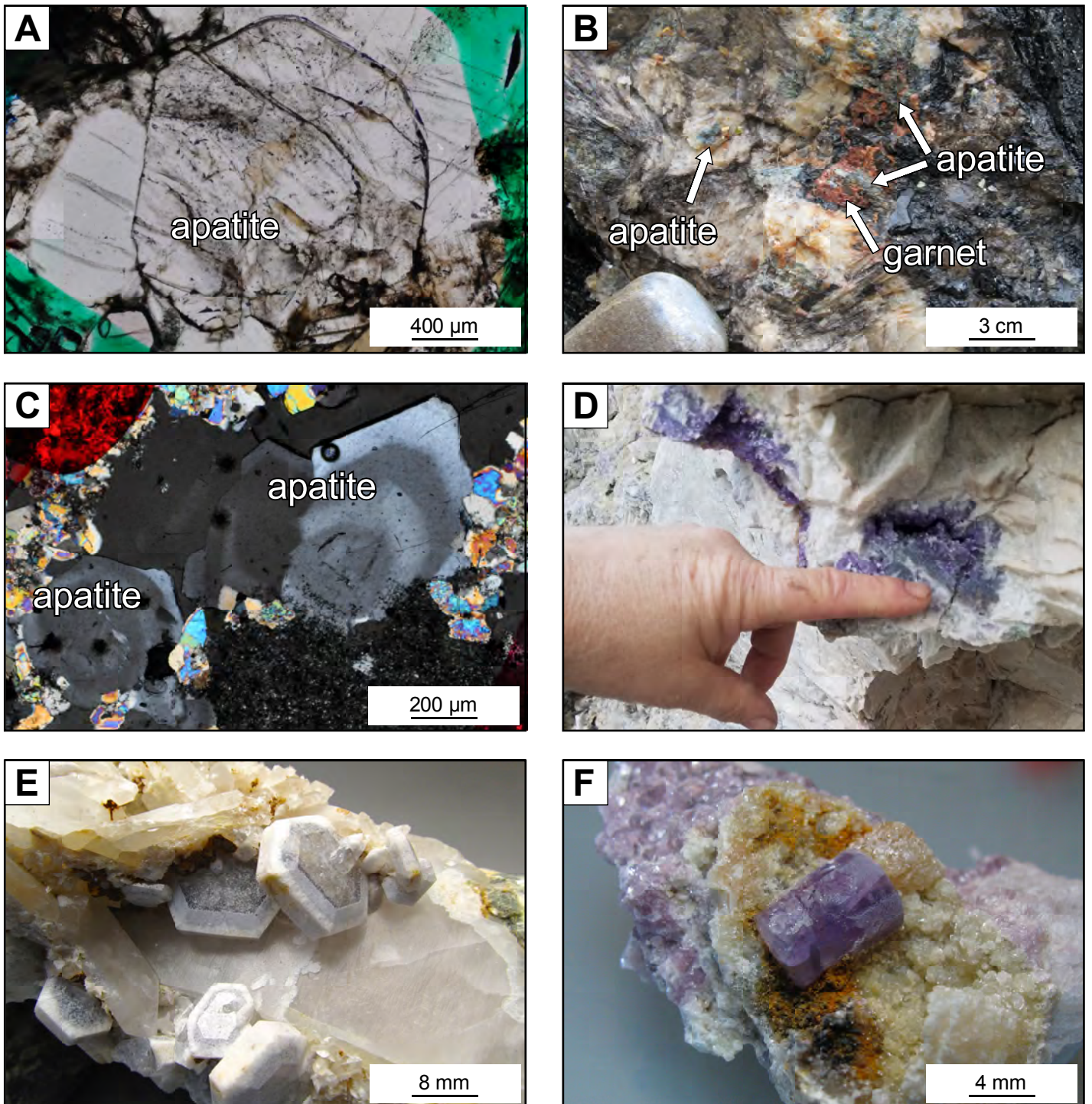


Fig. 3

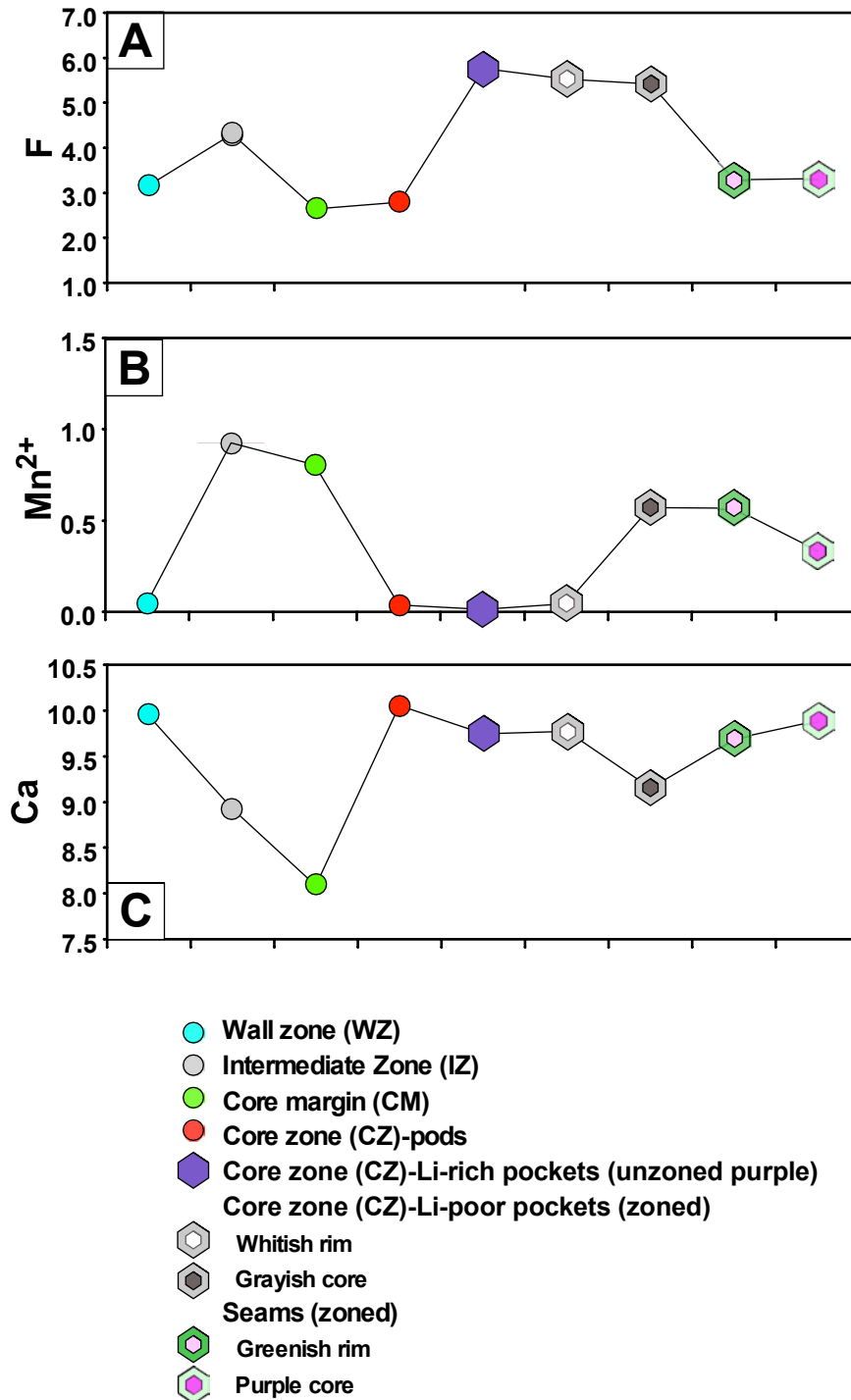


Fig. 4

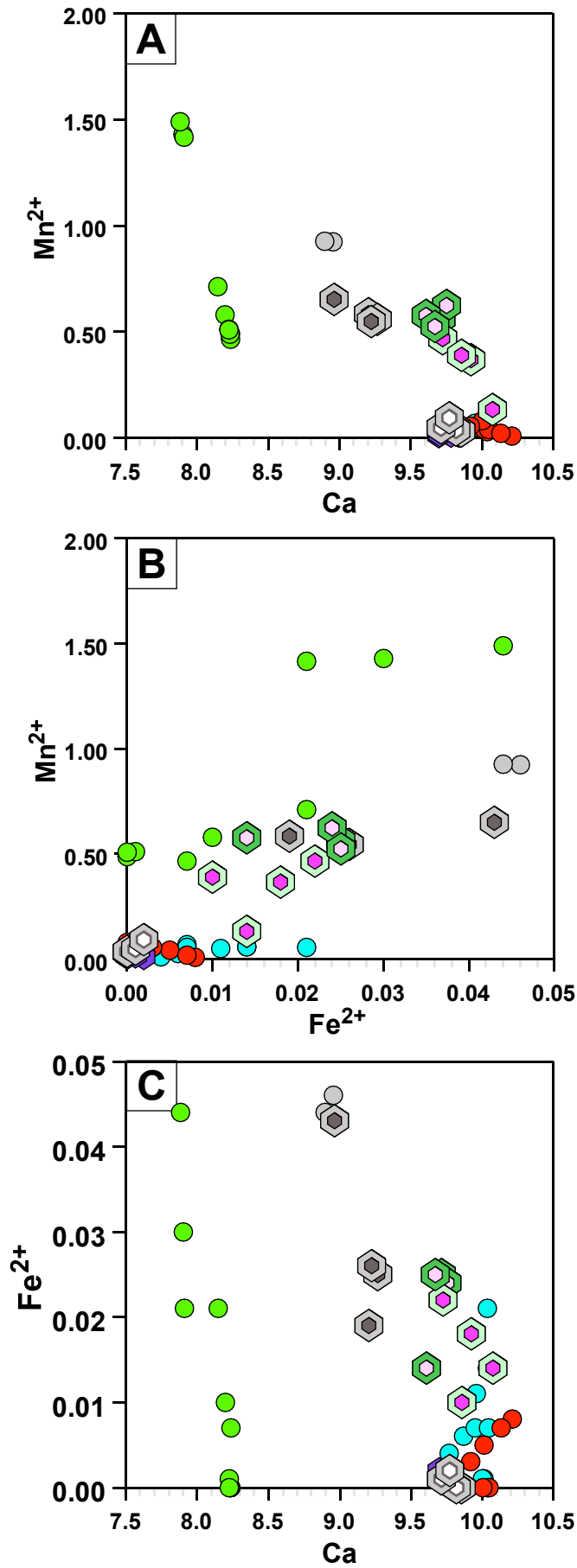


Fig. 5

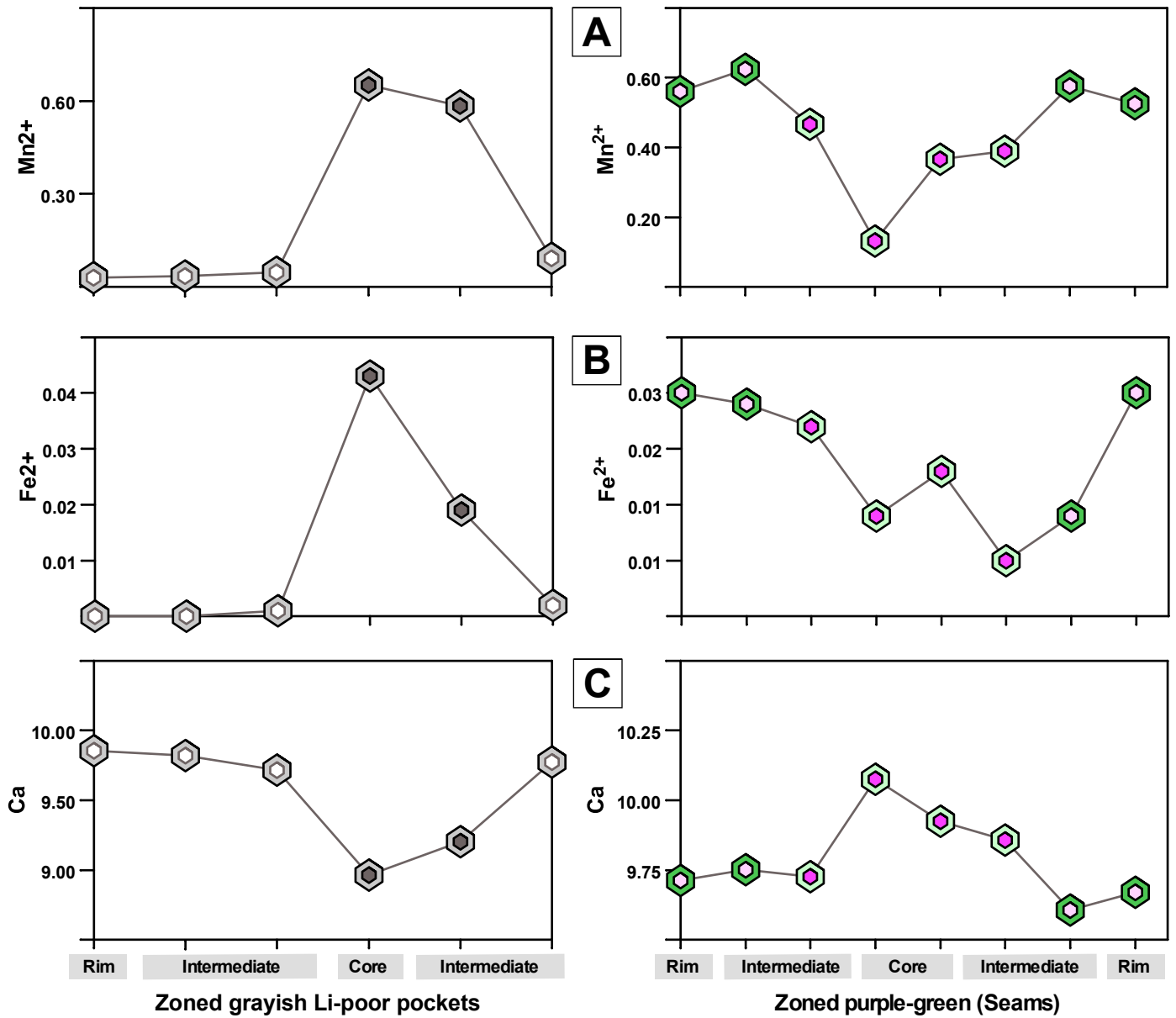


Fig. 6

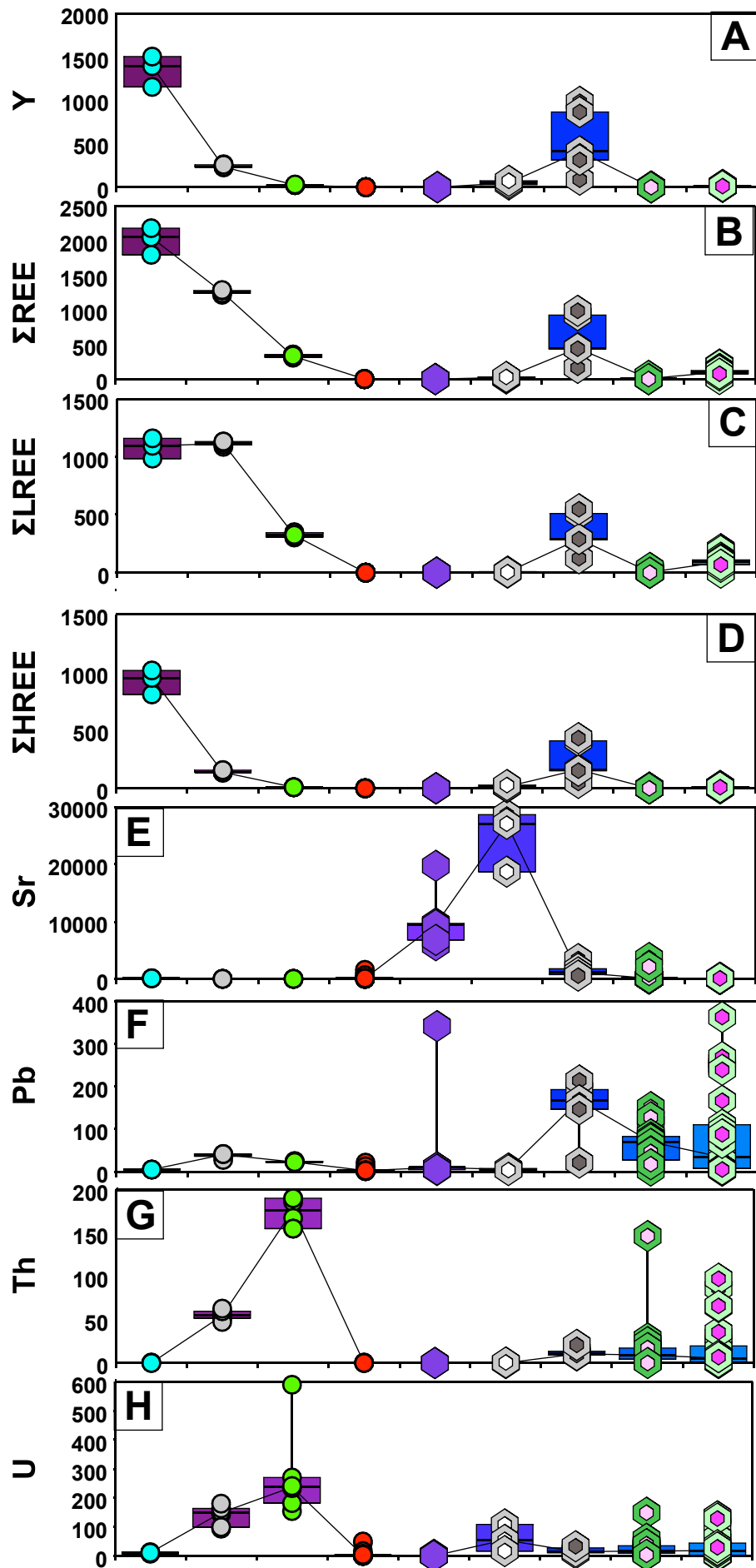


Fig. 7

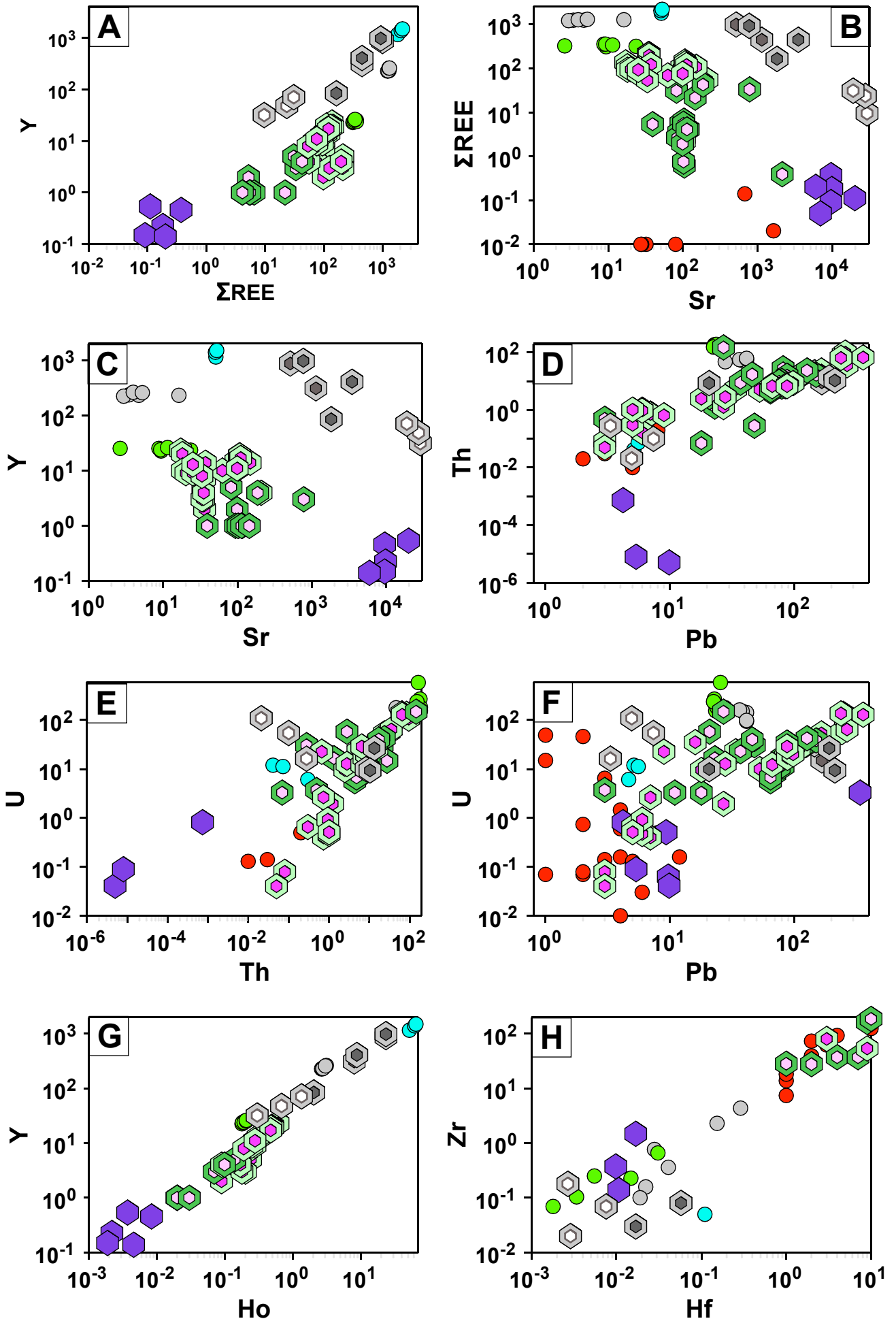


Fig. 8

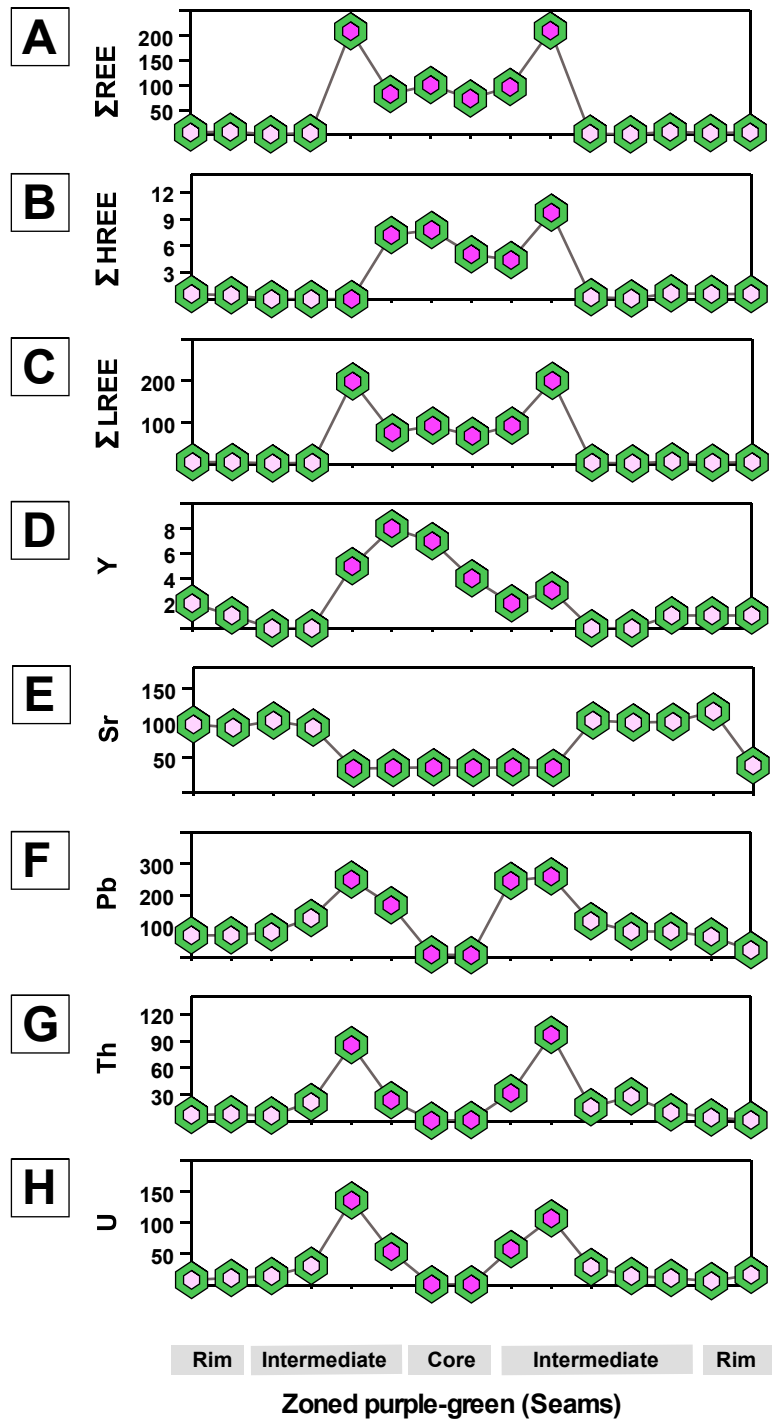
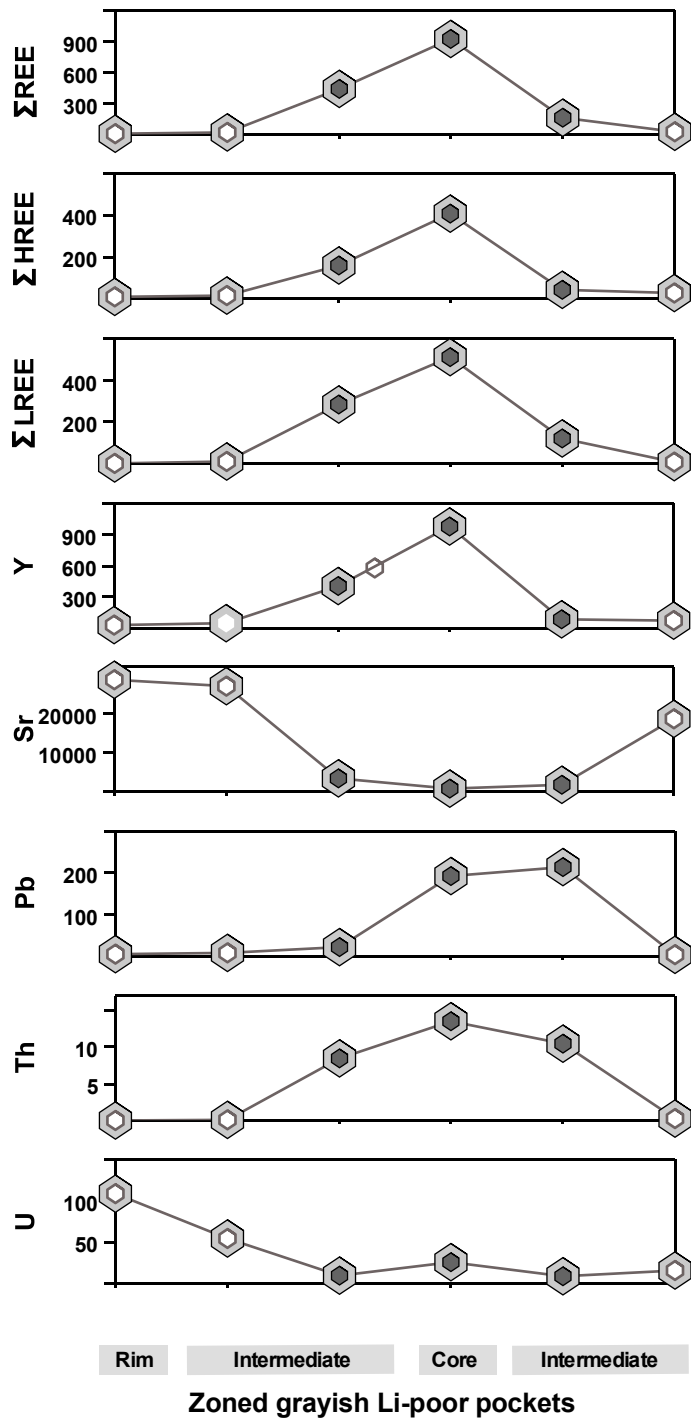


Fig. 9

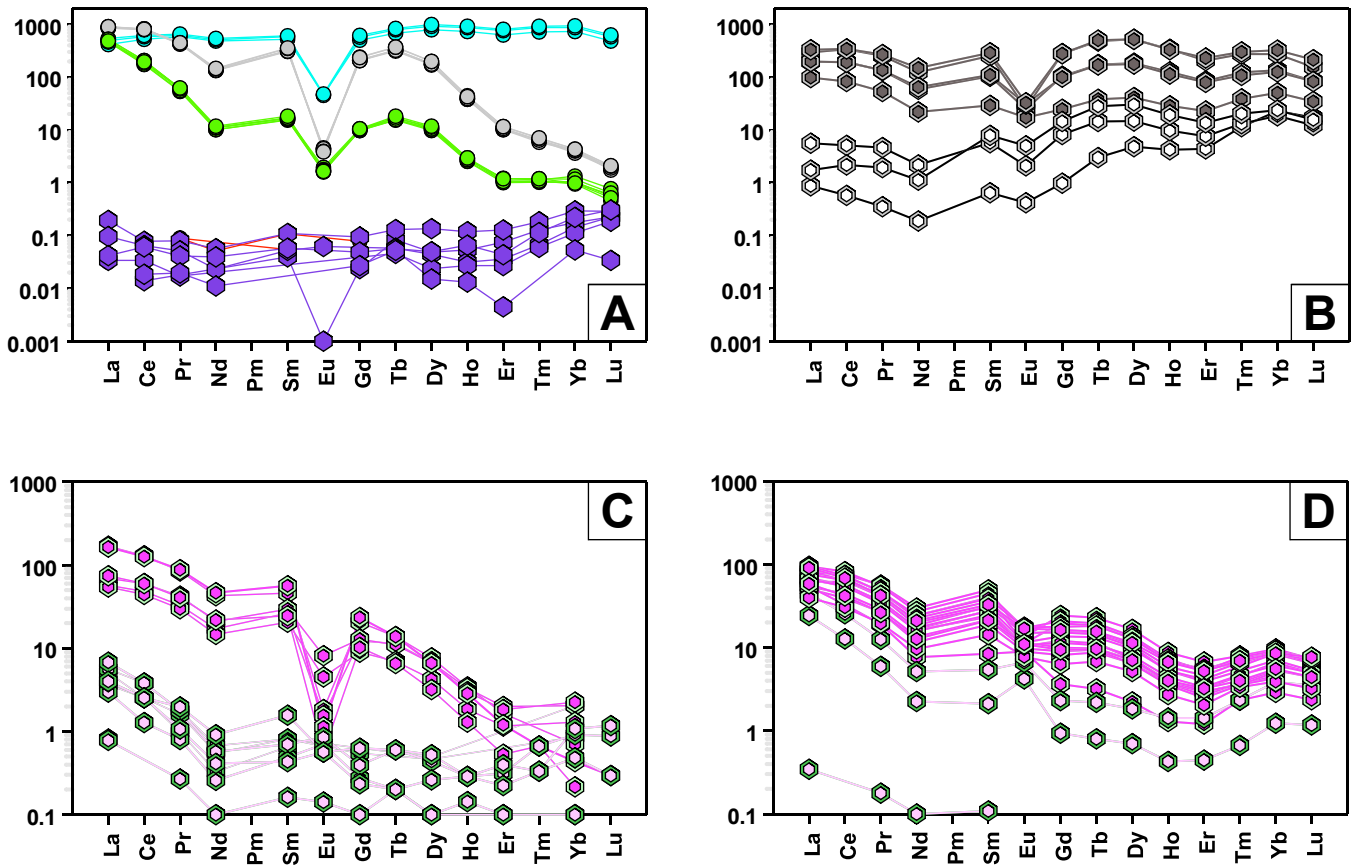


Fig. 10

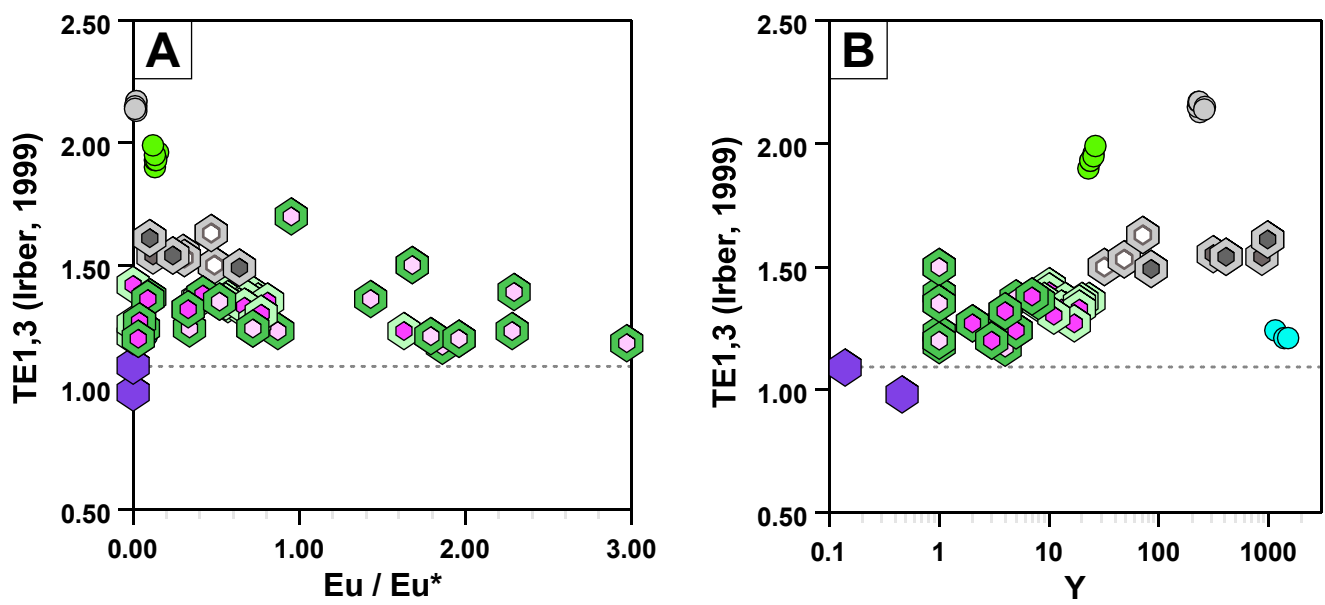


Fig. 11

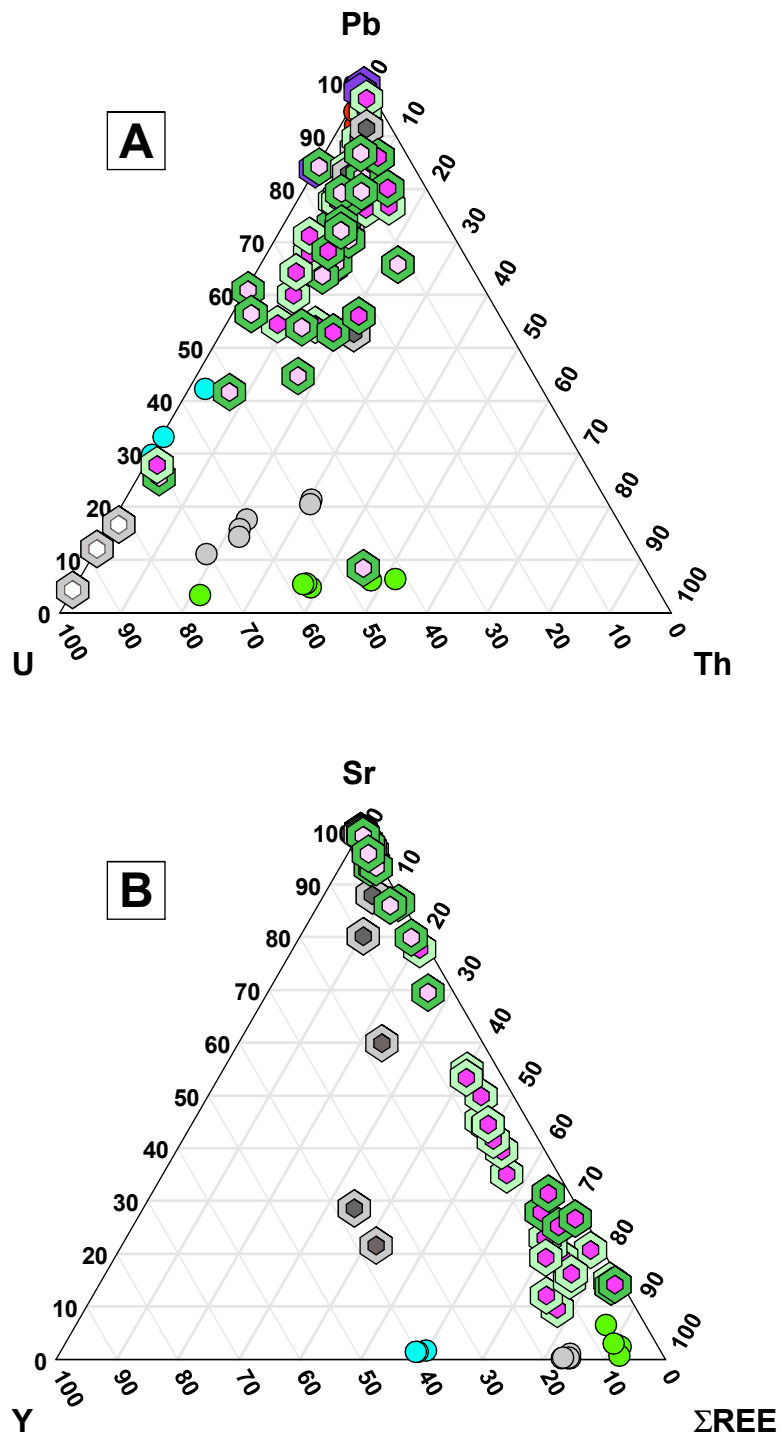


Fig. 13

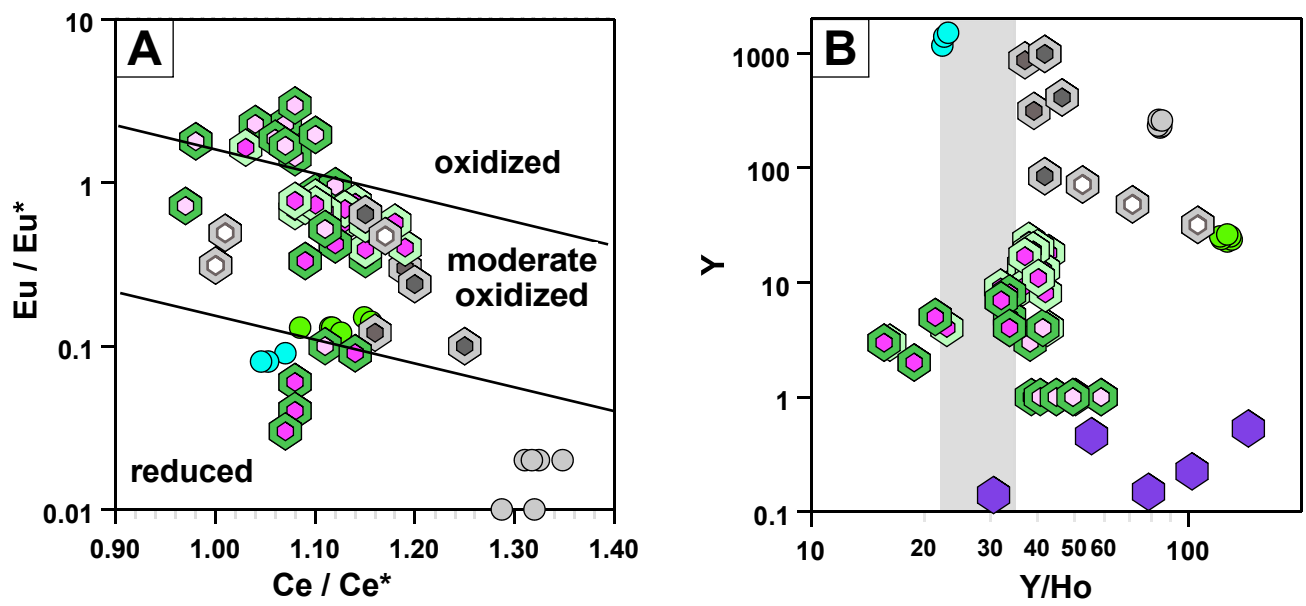


Fig. 12